

Université du Québec  
Institut National de la Recherche Scientifique

**Synthesis of  $\text{Ca}_x\text{Ba}_{1-x}\text{Nb}_2\text{O}_5$  Thin Films on Lattice Matched  $\text{Gd}_3\text{Ga}_5\text{O}_{12}$   
substrate by Pulsed Laser Deposition**

By  
S M Humayun Kabir

Mémoire présentée pour l'obtention du grade de  
Maître ès sciences (M.Sc.)

**Jury d'évaluation**

Président du jury et  
examineur interne

Professor Andreas Peter Ruediger  
INRS Energie Matériaux Télécommunications

Examineur externe

Professor Anne-Marie Kietzig  
Department of Chemical Engineering  
McGill University, Canada

Directeur de recherché

Professor Mohamed Chaker  
INRS Energie Matériaux Télécommunications

## Abstract

The accelerating increase in information traffic demands higher data transfer for the telecommunications. Thin film materials with high electro-optic (EO) coefficient are attractive towards the fabrication of high performance photonic devices, such as EO modulators for telecommunications applications. The ferroelectric Tetragonal Tungsten Bronze (TTB) family material  $\text{Sr}_x\text{Ba}_{1-x}\text{Nb}_2\text{O}_6$  (SBN) has shown high electro-optic coefficient both in the bulk and thin film form. With compared to commercially available conventional lithium niobate ( $\text{LiNbO}_3$ , LN), SBN has forty times higher electro-optic coefficient. But, due to the low Curie temperature (below  $80^\circ\text{C}$ ) SBN is not suitable to use as active layer in EO modulators operating at hundreds of GHz. On the other hand,  $\text{Ca}_x\text{Ba}_{1-x}\text{Nb}_2\text{O}_6$  (CBN), which also belongs to TTB family has high electro-optic coefficient (130 pm/V) and Curie temperature (above  $200^\circ\text{C}$ ), and hence a potential candidate for next generation electro-optic devices applications. Epitaxial CBN thin films have been synthesized on various substrates including MgO, Nb:SrTiO<sub>3</sub>, as well as on Silicon. However, epitaxial CBN films have to be achieved on a lattice matched and device fabrication compatible substrates (refractive index of the substrate should be lower than that of CBN) before they can be integrated in high-performance devices. This work focuses on the synthesis of CBN thin films on lattice matched Gadolinium Gallium Garnet ( $\text{Gd}_3\text{Ga}_5\text{O}_{12}$ , GGG) substrate.

In the first part of our work, we have investigated structural and optical properties of CBN thin film. In our experiment, we have done the optimization of CBN thin film on GGG substrate. XRD, XPS and AFM measurements were performed for the structural, compositional, and surface properties measurements. After that ellipsometric measurements were taken for the

optical properties analysis. We found a high optical transmittance of 85% for epitaxial CBN films deposited at a 50 mTorr oxygen pressure.

The promise of nanophotonic devices is controlled by the large size difference between much smaller photonic waveguides and comparatively large optical fibers, which causes an unacceptable amount of loss without a mode size conversion solution. One such solution to overcome the huge loss is the vertical grating coupler which allows light to be efficiently coupled from the top of a device. In the second part of our work, we have successfully fabricated and demonstrated light coupling through a CBN thin film based optical grating coupler to CBN thin film based waveguides on GGG substrate.

# Acknowledgement

I would like to express my deep sense of gratitude and sincere thanks to my supervisor Professor Mohamed Chaker for giving me the opportunity to accomplish my graduate studies under his kind supervision at Institut National de la Recherche Scientifique (INRS), Université du Québec, Canada. I sincerely acknowledge his support during all sorts of hurdles in the execution of my thesis work. I would like to thank the jury members, Professor Andreas Peter Ruediger, and Professor Anne-Marie Kietzig for their useful thoughts and comments which really helped me to improve my thesis.

Being far away from home for such a long period of time is certainly not easy unless you have various good people around to show you the do's and don'ts. I was indeed blessed with so many nice people from both my and other research groups at INRS. Specially, I would like to thank Dr. Nadir Hossain for guiding me throughout my master study. Thanks to my friends and colleagues from INRS-EMT, whom I worked with in the cleanroom. I would like to thank Dr. Boris Le Drogoff, Dr. Sébastien Delprat, and Amine Zitouni (thanks for the clean-room help). I would like to thank Christophe Chabanier for all the XRD and XPS measurement.

I wish to thank my parents and my brothers and sister, for the support and love they gave me over the years. Being away from home for more than 14 years, you have been my strength. Finally, I would like to thank my better half Shamsun Nahar, for being by my side and coping with all my tensions.

July 29, 2017

S M Humayun Kabir

# Table of contents

<b>Abstract.....</b>	<b>ii</b>
<b>Acknowledgement.....</b>	<b>iv</b>
<b>Table of contents.....</b>	<b>v</b>
<b>List of figures.....</b>	<b>viii</b>
<b>List of tables.....</b>	<b>xi</b>
<b>List of abbreviations.....</b>	<b>xii</b>
<b>List of symbols.....</b>	<b>xiii</b>
<b>List of publications.....</b>	<b>xiv</b>
<b>Chapter 1: Introduction.....</b>	<b>1</b>
1.1 Introduction.....	1
1.2 What is ferroelectric material?.....	3
1.3 Properties of ferroelectric thin films.....	7
1.4 Applications of ferroelectric material.....	10
1.5 Challenges for deposition and device application.....	14
1.6 Structure of the thesis.....	17
1.7 References.....	20
<b>Chapter 2: Growth and Characterization Techniques of Thin Films.....</b>	<b>23</b>
2.1 Growth techniques of thin films.....	23
2.1.1 Pulse laser deposition (PLD) of typical perovskite thin films.....	23
2.2 Characterization Methods.....	27
2.2.1 X-ray Diffraction (XRD).....	28
2.2.2 Atomic Force Microscopy (AFM).....	29

2.2.3 Scanning Electron Microscopy (SEM).....	32
2.2.4 Energy Dispersive X-Ray Spectroscopy (EDS or EDX).....	34
2.2.5 X-ray Photoemission Spectroscopy (XPS).....	37
2.3 Electron-beam lithography.....	40
2.4 Inductively Coupled Plasma (ICP) Etcher.....	41
2.5 Comparison of the characterization techniques.....	44
2.6 Conclusion.....	44
2.7 References.....	45
<b>Chapter 3: CBN Thin Film Deposition and Optimization.....</b>	<b>47</b>
3.1 Substrate choice.....	47
3.2 Sample cleaning.....	49
3.3 CBN thin film deposition.....	51
3.4 Experimental results.....	53
3.4.1 Structure and morphology.....	53
3.4.1.1 XRD Analysis.....	53
3.4.1.2 AFM Analysis.....	56
3.4.1.3 SEM Analysis.....	58
3.4.1.4 XPS analysis.....	59
3.4.2 Optical properties.....	61
3.5 Conclusion.....	62
3.6 References.....	63
<b>Chapter 4: Grating Coupler Fabrication.....</b>	<b>65</b>
4.1 Introduction.....	65

4.2 Grating coupler fabrication procedures.....	66
4.3 Grating coupler characterizations.....	69
4.4 Conclusion.....	71
4.5 References.....	72
<b>Chapter 5: Conclusion and Future Work.....</b>	<b>73</b>
<b>Résumé en Français.....</b>	<b>75</b>

## List of figures

Figure 1.1: LiNbO <sub>3</sub> modulator (source: www.oclaro.com).....	2
Figure 1.2: Venn diagram showing how ferroelectrics fit into the different classes of the dielectric materials.....	5
Figure 1.3: Typical polarization curve of a ferroelectric material.....	6
Figure 1.4: Applications of ferroelectric thin film based devices.....	11
Figure 1.5: Generation of photo charge carriers in a typical ferroelectric thin film under illumination.....	13
Figure 2.1: Schematic illustration of the pulsed laser deposition (PLD) setup.....	25
Figure 2.2: X-rays diffraction through a periodic arrangement of planes of atoms.....	28
Figure 2.3: (a) Schematic representation of the AFM (b) Force regimes governing the AFM measurement.....	30
Figure 2.4: Schematic representation of SEM.....	33
Figure 2.5: EDS Spectrum for Alloy MP35N.....	36
Figure 2.6: 60 nm width posts of negative ebeam resist (maN2403) .....	41
Figure 2.7: Inductively Coupled Plasma (ICP) Etching System.....	42
Figure 2.8: (a). Nanometric-anisotropic etching of SiO <sub>2</sub> (30nm lines and spaces grating) for Nanoimprint applications, (b). Anisotropic etching of GaAs (80nm width trenches, resist mask still in place) .....	43
Figure 3.1: AFM images of GGG substrates cleaned by acetone and IPA. Scan area (a) 1 μm and (b) 5 μm.....	50

Figure 3.2: AFM images of GGG substrates cleaned by acetone, IPA, buffered oxide etch (BOE) cleaning. Images are taken after 1000 °C annealing in oven. Scan area (a) 1 μm and (b) 5 μm.....	50
Figure 3.3: SEM image of GGG sample surface before cleaning.....	51
Figure 3.4: CBN thickness calibration by SEM.....	52
Figure 3.5: CBN thickness calibration by Dektak profilometer.....	52
Figure 3.6: XRD θ-2θ scans of CBN/GGG thin films grown on (001) oriented GGG substrate at the growth temperate of 500° C, 600° C, 700° C, and 750° C. Other deposition parameters such as pressure 1 mTorr and fluence 2 J/cm <sup>2</sup> were kept same for all depositions during deposition temperature optimization. Y-axis is in logarithmic scale and offsets are created for better representation.....	54
Figure 3.7: XRD θ-2θ scans of CBN/GGG thin films grown on (001) oriented GGG substrate under the oxygen partial pressure of 1, 50 and 100 mTorr. Other deposition parameters such as temperature 750° C and fluence 2 J/cm <sup>2</sup> were kept same for all depositions during deposition pressure optimization. Y-axis is in logarithmic scale and offsets are created for better representation.....	55
Figure 3.8: Rocking curve measurements of CBN deposited under three different temperatures. Other deposition parameters such as pressure 1 mTorr and fluence 2 J/cm <sup>2</sup> were kept same for all depositions.....	56
Figure 3.9: (a) (3x3 μm) AFM image of the CBN/GGG surface at 1 mTorr and (b) corresponding 3D view. (c) AFM image of sample deposited at 50 mTorr. (d) AFM image of sample deposited at 100 mTorr. Deposition temperature 750 °C and fluence 2 J/cm <sup>2</sup> were kept constant for all....	57

Figure 3.10: SEM top view image of the CBN films (deposited at 750°C and 50 mTorr) on GGG substrate.....	59
Figure 3.11: XPS spectra of the CBN films (deposited at 750°C and 50 mTorr) on GGG substrate.....	60
Figure 3.12: Optical transmittance of CBN thin film on GGG substrate with the variation of deposition pressure (1, 50, and 100 mTorr). Keeping all other deposition pressure same (temperature 750° C, fluence 2 J/cm <sup>2</sup> , frequency 20 Hz etc) .....	61
Figure 4.1: Total loss as a function of waveguide length to estimate the facet loss and propagation loss. (inset) Typical mode profile at the output of the waveguide.....	66
Figure 4.2: Schematic representation of CBN etching for grating coupler fabrication on GGG..	67
Figure 4.3: SEM image of electroplated Ni mask.....	68
Figure 4.4: Block diagram of optical grating coupler characterization setup.....	69
Figure 4.5: (a) Total loss as a function of wavelength for various waveguide lengths measured by LUNA vector analyzer system. (b) Total loss as a function of waveguide length.....	70

## List of tables

Table 1-1: The seven crystal systems in three dimensions.....	3
Table 2-1: Comparison of all presented characterization techniques.....	44
Table 3-1: Comparison of different substrates for CBN deposition.....	48
Table 3-2: Roughness comparison between two different types of substrate cleaning.....	50
Table 3-3: Roughness comparison of CBN films under different growth condition.....	58
Table 3-4: Elemental quantification (% Atomic Concentration) of CBN measured by XPS.....	60

## List of abbreviations

<i>Abbreviations</i>	<i>Description</i>
AFM	Atomic Force Microscopy
CBN	Calcium Barium Niobate
CSD	Chemical Solution Deposition
EDS	Energy Dispersive X-Ray Spectroscopy
EO	Electro-Optic
FEPV	Ferroelectric Photovoltaic
FeRAM	Ferroelectric Random Access Memory
GGG	Gadolinium Gallium Garnet
ICP	Inductively Coupled Plasma
RIE	Reactive Ion Etching
LN	Lithium Niobate
MBE	Molecular Beam Epitaxy
MOCVD	Metal Organic Chemical Vapour Deposition
PLD	Pulsed Laser Deposition
SBN	Strontium Barium Niobate
SEM	Scanning Electron Microscopy
TTB	Tetragonal Tungsten Bronze
XPS	X-ray Photoemission Spectroscopy
XRD	X-ray Diffraction

## List of symbols

<i>Abbreviations</i>	<i>Description</i>
$P_r$	Remnant Polarization
$E_c$	Coercive Field
$D$	electric flux density
$C$	Curie constant
$T$	Temperature (in Kelvin)
$T_c$	Curie Temperature
$S$	Mechanical Strain
$s^E$	elasticity coefficient
$\epsilon^T$	permittivity
$\epsilon$	Dielectric Constant
$p_i$	Pyroelectric Coefficient
$r_{ijk}$	Pockels Electro-Optic Coefficient
$S_{ijkl}$	Kerr Electro-Optic Coefficient
$\eta$	Tensor
$\lambda$	Wavelength
$\theta$	Diffraction Angle

# List of publications

## Journals:

1. Sébastien Vigne, Nadir Hossain, Faezeh Fesharaki, **S. M. Humayun Kabir**, Joëlle Margot, Ke Wu, and Mohamed Chaker, "Optical properties of epitaxial  $\text{Ca}_x\text{Ba}_{1-x}\text{Nb}_2\text{O}_6$  thin film based rib-waveguide structure on (001) MgO for electro-optic applications", *Optics Express*, Vol. 24, Issue 25, pp. 28573-28582 (2016).
2. S. Vigne, N. Hossain, **S.M. Humayun Kabir**, J. Margot, K. Wu, and M. Chaker, "Structural and optical properties of  $\text{Ca}_x\text{Ba}_{1-x}\text{Nb}_2\text{O}_6$  thin films deposited by radio frequency magnetron sputtering", *Optical Materials Express*, Vol. 5, Issue 11, pp. 2404-2414 (2015).

## Conferences:

1. **S. M. Humayun Kabir**, N. Hossain, S. Vigne, F. Fesharaki, K. Wu, J. Margot, and M. Chaker, "Synthesis of CBN/GGG Thin Film Materials for Device Applications", Plasma-Quebec 2017, Montreal, QC, Canada.
2. **S. M. Humayun Kabir**, N. Hossain, F. Fesharaki, K. Wu, J. Margot and M. Chaker "Pulsed Laser Deposition of  $\text{Ca}_x\text{Ba}_{1-x}\text{Nb}_2\text{O}_6$  thin film on GGG substrate" Plasma-Quebec 2016, Montreal, QC, Canada.
3. **S. M. Humayun Kabir**, N. Hossain, S. Vigne, F. Fesharaki, K. Wu, J. Margot and M. Chaker, "Synthesis of CBN Thin Film Materials for Electro-Optic Device Applications", Plasma-Quebec 2015, Montreal, QC, Canada.

4. **S. M. Humayun Kabir**, N. Hossain, S. Vigne, and M. Chaker, "CBN Thin Film Materials for Electro-Optic Device Applications", Photonics North 2015, Ottawa Shaw Centre, Ottawa, Canada. June 9 ~ 11, 2015.

# Chapter1

## Introduction

This chapter provides an overview of the research carried out throughout the master's study. First, a brief introduction of ferroelectric material is given. Secondly, descriptions of ferroelectric materials are given. Thirdly, a brief review of the properties of ferroelectric material is presented followed by the application of ferroelectric thin film. Then, the challenges of ferroelectric thin film deposition and fabrication are discussed. Finally, the structure of the thesis is presented where the content of each individual chapter is briefly addressed.

### 1.1 Introduction

Ferroelectric materials have been widely studied over the past few decades because of the excellent ferroelectric, piezo-electric, pyro-electric, and electro-optic properties [1-4]. Ferroelectric materials are suitable for the applications in capacitors, actuators, and electro-optic modulators, etc. Recent advances in material deposition technologies show ferroelectric material synthesis on suitable substrates provide excellent structural and optical properties [5]. Ferroelectric material based optical ridge waveguide on silicon substrate has been designed, fabricated and characterized for future integrated electro-optic devices [6]. Other interesting properties of ferroelectric materials such as the nonlinear optical properties are also explored using second harmonic generation, which shows its potential for integrated nonlinear prism or optical frequency converter for on-chip devices [7]. Although, ferroelectric materials are widely studied for electronic applications, the increasing demand for higher data communications

bandwidth and lower power consumption telecom devices has made great interest towards the use of electro-optically active ferroelectric thin films in the optical domain. Integrated optical devices compatible with electronic systems are necessary for optical data transmission. Due to the excellent nonlinear optical properties, ferroelectric oxides have been used for signal processing in optical communication systems. Also, strong electro-optic effect has made ferroelectric materials a key element for high-bandwidth electro-optic modulators in optical communication systems [8]. As an example, figure 1.1 shows a packaged LiNbO<sub>3</sub> modulator.



Figure 1.1: LiNbO<sub>3</sub> modulator (source: [www.oclaro.com](http://www.oclaro.com))

The use of external electro-optic modulator provides many advantages over directly modulating semiconductor laser such as wavelength variation, higher speed, etc. Although, high-bandwidth LiNbO<sub>3</sub> modulators have been already demonstrated but there are other ferroelectric materials which have even larger electro-optic coefficients that potentially promise higher bandwidth and lower voltage operation for device applications. Other ferroelectric materials such as LiTaO<sub>3</sub>, KNbO<sub>3</sub>, (Ba,Sr)TiO<sub>3</sub>, BaTiO<sub>3</sub>, PZT, CBN-27, and SBN-75 have been considered for such applications. However, it is very difficult to grow large area bulk single crystals which severely limited their utilization in practical devices. Furthermore, bulk single crystals are not suitable for applications in integrated photonic circuits or optical interconnects.

## 1.2 What is ferroelectric material?

Before discussing ferroelectric material, it is useful to know the class of insulating materials that form dielectrics. Materials that will sustain a dielectric polarisation under the application of an applied electric field are called dielectric materials.

Based on the atomic lattice or structure, crystal systems are classified in seven categories. The atomic lattice is a three dimensional network of atoms that determines which crystal system the material belongs to, as well as its physical properties and appearance. If a crystal structure has a center of symmetry, it means that for a point within a crystal with respect to which similar planes and edges are symmetrical in opposite pairs. A list of non-centrosymmetric, or acentric, crystal groups is given in table 1-1.

**Table 1-1:** The seven crystal systems in three dimensions (Sébastien Vigne, PhD thesis)

Crystal System	Polar (acentric)	Nonpolar (acentric)	Lattice Parameters	angles
Triclinic	1	-	$a \neq b \neq c$	$\alpha \neq \beta \neq \gamma \neq 90^\circ$
Monoclinic	2, m	-	$a \neq b \neq c$	$\alpha = \gamma = 90^\circ, \beta \neq 90^\circ$
Orthorhombic	mm2	222	$a \neq b \neq c$	$\alpha = \beta = \gamma = 90^\circ$
Trigonal	3m, 3	32	$a = b = c$	$\alpha = \beta = \gamma \neq 90^\circ$
Tetragonal	4mm, 4	$\bar{4}, 422, \bar{4}2m$	$a = b \neq c$	$\alpha = \beta = \gamma = 90^\circ$
Hexagonal	6mm, 6	$\bar{6}, \bar{6}m2$	$a = b \neq c$	$\alpha = \beta = 90^\circ, \gamma = 120^\circ$
Cubic	None	23, $\bar{4}3m, 432$	$a = b = c$	$\alpha = \beta = \gamma = 90^\circ$

All of the crystalline materials whose structures possess these point groups (with the exception of 432) exhibit the phenomenon of piezoelectricity, which means that stress will generate a charge separation on the faces of the crystal (the direct piezoelectric effect) and will undergo mechanical strain when subjected to an electric field (the converse piezoelectric effect) [9]. A sub-set of the non-centrosymmetric crystals also possess a unique axis of symmetry which are said to be *polar*. Polar crystals are piezoelectric and also show pyroelectricity. Pyroelectricity is the property of certain crystals which have spontaneous polarization. Alternatively, pyroelectricity is interpreted as the ability of certain materials which can generate a temporary voltage under heating or cooling. Polar crystals also have built-in dielectric polarisation to the unit cell of the crystal structure which is called *spontaneous polarisation*. The application of stress (for piezoelectric) or a change in temperature (for pyroelectric) causes a change in the dipole moment which results in the charge separation on the surface of the crystal. The direction and magnitudes of the spontaneous polarisation in a polar dielectric can be changed by the application of an electric field but it will return to its zero-field value upon removal of the applied electric field.

A sub-set of the set of polar dielectrics exists for which the spontaneous polarisation can be switched to a different, stable direction with the application of an electric field of sufficient magnitude. In this case, the polarisation will not spontaneously return to its original direction and magnitude even after removal of the electric field. These crystals are called ferroelectric. The relationships between the sets of ferroelectric, polar, acentric, and centrosymmetric dielectrics are shown in the following Venn diagram in Figure 1.2.

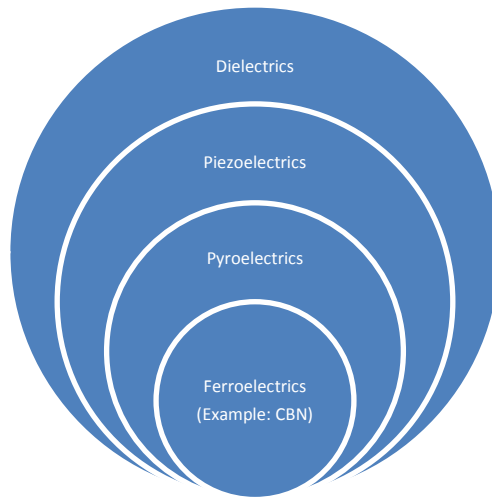


Figure 1.2: Venn diagram showing how ferroelectrics fit into the different classes of the dielectric materials.

Ferroelectric materials are characterized by their ability to reverse polarization with an applied electric field. This is measured experimentally represents a polarization curve (hysteresis curve) that allows measuring some typical quantities as ferroelectric polarization saturation, residual and coercive. Figure 1.3 shows the hysteresis curve for ferroelectric material. At position O, the domains are polarized randomly, and the measured macroscopic polarization is close to zero. If the intensity of the electric field ( $E$ ) is gradually increased, the polarization ( $P$ ) rise to a maximum, or saturation, value at which all the domains are aligned in the same direction (A). When the electric field is diminished, the polarization decreases, again lagging behind the change in field strength  $E$ . In fact, when applied electric field decreased to zero (B), the material still remained polarized and  $P$  has a certain value. The polarization that remaining in the material even after the polarization field is reduced to zero, is called the remnant polarization ( $P_r$ ). The application of reverse electric field wipe out the remnant polarization and the curve intersects the horizontal axis ( $E$ ) to an electric field value called Coercive field ( $E_c$ ), which is the minimum

field to be applied to reverse the ferroelectric domain. If the electric field is continued to be applied in the same direction, the domain will again all be aligned in the opposite direction and polarization will reach saturation (D). At this point, if the electric field is increased the polarization cycle will be closed through the point of negative remnant polarization and of positive coercive field.

If we continue the cycle, the fields will again all be aligned in the opposite direction and polarization will reach saturation. The cycle is closed and performing again the increase in the electric field to saturation through the point of negative remnant polarization ( $-Pr$ ) and of positive coercive field ( $E_c$ ).

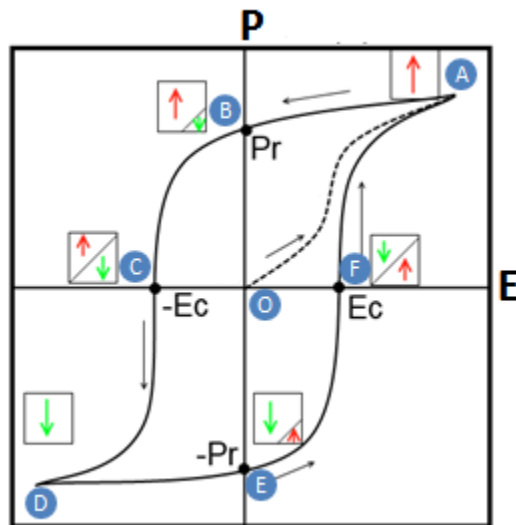


Figure 1.3: Typical polarization curve of a ferroelectric material (Sébastien Vigne, PhD thesis).

Ferroelectric materials have a transition temperature called the Curie temperature and beyond this temperature they lose their ferroelectric properties and become paraelectric. After this

transition temperature, their dielectric constant follows the Curie-Weiss law of which is described below [10]

$$\varepsilon = \varepsilon_0 + \frac{C}{T - T_c}$$

where,  $\varepsilon$  is the dielectric constant,  $C$  is a material-specific Curie constant,  $T$  is absolute temperature (in Kelvin), and  $T_c$  is the Curie temperature (in Kelvin). There are some materials having Curie temperature greater than their melting point which keeps their ferroelectric state permanently. CBN is one of them which has Curie temperature of 280° C. This property has made CBN a good candidate for practical application.

### 1.3 Properties of ferroelectric thin films

A perovskite is any material with the same type of crystal structure as in  $\text{CaTiO}_3$ . In general, the chemical formula of a perovskite is  $\text{ABX}_3$ , with oxygen at the face centered. **A** and **B** are cations with different sizes and **X** is the anion that bounds to both. The **A** atoms are larger than **B** atoms. Perovskite based thin films are used for a wide variety of applications based on their piezoelectric, ferroelectric, pyroelectric and electro-optic properties. This section briefly reviews the properties of the ferroelectric thin films and their applications.

**Piezoelectric properties:** Piezoelectricity refers to the coupling between mechanical and electrical behaviour of a material. Ferroelectric materials result strain in it under tensile or compressive forces. This strain generates an electrical charge inside the materials. This phenomenon is called piezoelectric effect [11]. On the contrary, when an electrical field is applied, strain is created together with resulting stress. This phenomenon is called converse

piezoelectric effect. The relationships between the electrical and elastic properties can be expressed as bellow:

$$D = d * T + \epsilon^T * E$$

$$S = S^E * T + d * E$$

where  $D$ ,  $E$ ,  $T$ ,  $S$ ,  $d$ ,  $s^E$ , and  $\epsilon^T$  represents the electric flux density, electric field, mechanical stress, mechanical strain, piezoelectric charge coefficient, elasticity coefficient (when  $E$  is constant), and permittivity (when  $T$  is constant) respectively. In spite of complex fabrication technique, a wide variety of devices based on piezoelectric film are fabricated, tested and analysed for comprehensive evaluation of their potential and limitations. This includes ultrasonic micromotors, acoustic sensors, AFM cantilevers, radio frequency and optical switches, and ultrasonic transducers for medical and sonar applications.

**Ferroelectric properties:** ferroelectricity refers to the properties of a material that has a spontaneous dipole moment which leads to a macroscopic polarization. In most ferroelectric materials the dipole moments are averaged to zero polarization when no fields are applied. The polarization can be reoriented or reversed with an applied electric field. Usually, ferroelectric properties of thin films are measured with a polarization-electric field hysteresis loop. Electrical switching of the ferroelectric domains creates the electrical hysteresis. The electrical hysteresis of the films is used for the application of ferroelectric random access memory (FRAM). This FRAM's not only writes data hundred times faster than conventional flash based micro controllers but also consume half the energy. The principle of non-volatile FRAMs is based on the polarization reversal by an external applied electric field of where the computational "0" and

“1” are represented by the non-volatile storage of the negative or positive remnant polarization state, respectively.

**Pyroelectric-properties:** Crystal structures are divided into thirty two classes. Of these thirty two, twenty exhibit direct piezoelectricity. Ten of these twenty piezoelectric classes exhibit a unique polar axis. All polar materials possess a spontaneous polarization and they are pyroelectric. A material is pyroelectric means that it's polarization can be changed as a result of temperature changes of the material [12]. When a pyroelectric material is heated, its dipole moments change which causes polarization to be changed as well. This change of polarization creates an electric potential difference. Although all ferroelectric materials do not exhibit pyroelectric properties but the best pyroelectric materials are all ferroelectric. The phenomenon of pyroelectricity is mostly used to detect infrared radiation. By utilizing the pyroelectric effect in thin film pyroelectric infrared detector arrays for thermal detection, objects and persons can be detected [13]. Perovskites such as  $\text{PbTiO}_3$  and PZT are preferred for this type of application because of their high pyroelectric coefficient, low dielectric loss, high resistivity, and high Curie temperature. The Pyroelectric coefficient may be represented as the change in the spontaneous polarization vector with temperature as [14]

$$p_i = \partial P_{s,i} / \partial T$$

where  $p_i$  is the vector for the pyroelectric coefficient.

**Electro-optic properties:** Certain materials change their optical properties when an external electric field is applied. This is caused by forces that distort the positions or shapes of the molecules forming the material which leads to changes in the optical properties of the medium.

The electro-optic effect is the change in the refractive index when an external dc or low-frequency electric field is applied. An electric field modifies refractive indices of an anisotropic electro-optic material and there by its effect on polarized light. The dependence of the refractive index on the applied electric field takes one of two forms [15]:

- Linear electro-optic effect: the refractive index changes in proportion to the applied electric field, also called the Pockels effect.
- Quadratic electro-optic effect: The refractive index changes in proportion to the square of the applied electric field, also called the Kerr effect

The propagation of the electromagnetic wave in a dielectric medium can be expressed in terms of the impermeability tensor  $\eta$ , which can be expanded in a taylor series about the applied electric filed  $E=0$  as bellow

$$\eta_{ij}(E) = \eta_{ij}^0 + \sum_k r_{ijk} E_k + \sum_{kl} S_{ijkl} E_{kl}$$

where  $i, j, k, l = 1, 2, 3$  and  $r_{ijk}$  and  $S_{ijkl}$  represent the Pockels and Kerr electro-optic coefficient.

## 1.4 Applications of ferroelectric material

Ferroelectric materials are widely used for numerous applications such as capacitors, piezoelectrics for ultrasound imaging and actuators, thermistors, switches known as transchargers or transpolarizers, oscillators and filters, varactors for RF/microwave circuits, high-k dielectrics, ferroelectric random access memory (FeRAM), ferroelectric tunnel junctions, multiferroic materials, piezoelectric transducers, pyroelectric detectors, light deflectors, modulators, and electro-optic materials for data storage applications. Some of the key

applications are described in sections. Figure 1.4 shows the applications of ferroelectric thin films for various types of electronic devices.

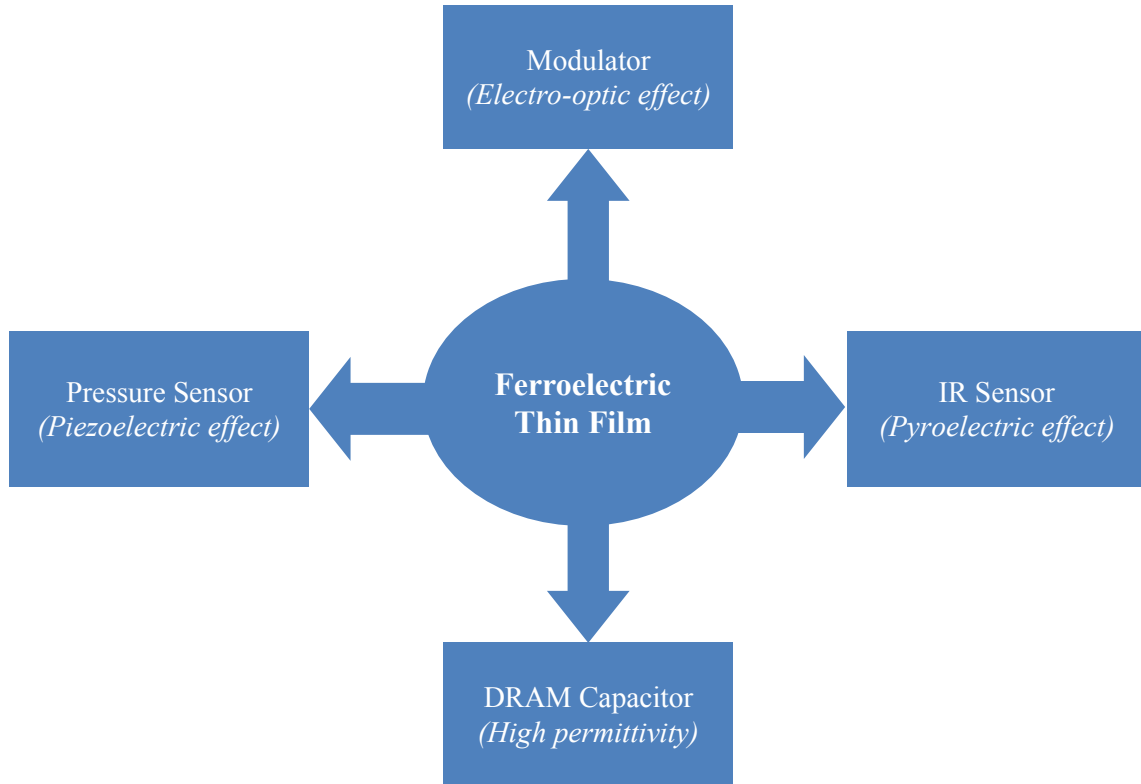


Figure 1.4: Applications of ferroelectric thin film based devices.

A ferroelectric capacitor consists of a pair of electrodes sandwiching a layer of ferroelectric material. Ferroelectric capacitors are tunable due to the nonlinear nature of the ferroelectric materials. The permittivity of ferroelectric material is easily tunable at the phase transition temperature. Because of this tunable property, physical sizes of ferroelectric capacitors are small in comparison to dielectric (non-tunable) capacitors of similar capacitance. The main application of this type of capacitor is in FeRAMs. In FeRAMs polarization is reversed by an external applied electric field of metal-ferroelectric-metal capacitors [16]. The nonvolatile storage of the

negative or positive remanent polarization state represents the computational “0” and “1”, respectively. Besides excellent electronic properties, FeRAMs have many attractive features like, read and write cycle times in the sub-100 ns range as well as low power consumption which make it superior to the performance of other nonvolatile technologies. Besides having a number of distinct advantages when compared to its competitors FeRAMs also have a number of disadvantages such as lower storage density, overall capacity limitation, and higher cost.

Another application of ferroelectric materials is in photo voltaic devices. In classical p-n junction based photovoltaic devices the effect of Schottky field might be present due to the electrodes. The effect of p-n junction mechanism is much higher than the Schottky effect. Therefore, the Schottky field effect is ignored in most of the literature. However there is another class of materials called ferroelectric materials which do not need p-n junctions to get photo carrier separation in the devices. In few homogeneous ferroelectric materials, charge separation occurs due to their innate crystal field. The polarity of crystals create microscopic electric fields across ferroelectric domains, separating photogenerated excitons into free charges, and segregating the transport of the free charges to reduce recombination rates. The polarization arises in ferroelectric oxides due to the crystal structure. Figure 1.5 shows the spontaneous polarization accompanied by a depolarizing field in the opposite direction separates the photo generated carriers and transports them effectively towards the respective electrodes

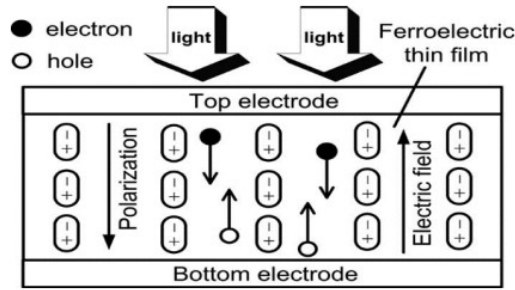


Figure 1.5: Generation of photo charge carriers in a typical ferroelectric thin film under illumination [17].

The magnitude of the polarization-induced internal electric field in ferroelectric photovoltaic (FEPV) materials is about one order of magnitude higher than that in a p-n junction based semiconductor devices [18]. Generally, the photovoltage in p-n junction based photo voltaic cells is determined by the difference of the quasi Fermi energy level of photocarriers, usually less than the bandgap ( $< 1\text{eV}$ ). The total open circuit voltage in the photo voltaic device is usually determined by the differences of work function between electrode-semiconductor-electrode interfaces. However, ferroelectric thin films offer additional advantages for photovoltaic devices, as they can modulate barrier heights at electrode-ferroelectric interfaces using the inherent spontaneous polarization charges thus tuning the magnitude of photo voltage in the structure [19]. Subject to the condition of materials engineering, ferroelectrics yield even above band gap photovoltage that clearly distinguishes them from conventional semiconductors, and is referred to as anomalous photovoltage [20]. The ferroelectricity driven photovoltaic effect is generally confirmed by reversing the direction of photocurrent using reverse polarization direction. However, the generation of photocurrent density is very poor typically in the order of  $\text{nA/cm}^2$  [21]. In addition, ferroelectrics refer to having extremely low mobility of charge carriers in the conduction band. Therefore, despite having improved device engineering and photocurrent

extraction technique [22], interest on ferroelectric photo voltaic has remained in academia rather than having commercial application.

One of the most important applications of ferroelectric thin films is in photonic devices. Since ferroelectric oxides have excellent nonlinear optical properties, they are widely used for signal processing in optical communication systems. Ferroelectric thin films have special application in optical modulator because of their strong electro-optic effect. As an example, LiNbO<sub>3</sub> is used for high-bandwidth electro-optic modulators in optical communication systems [8]. Most of the optical devices reported are based on single crystalline perovskite thin films epitaxially grown on MgO or SrTiO<sub>3</sub> substrates [23]. The state-of-art tunable photonic devices based on CMOS photonics platforms are based on two different approaches. It uses either electro-optic or piezoelectric properties of ferroelectric thin films. In case of an electro-optic modulator, the electro-optic effect is used to modulate a beam of light. Generally, the electro-optic effect changes the refractive index of a material resulting from the application of a low frequency electric field or a DC bias. The forces caused by the applied electric field distort the position, orientation, or shape of the molecules constituting the material. LiNbO<sub>3</sub> is the most popular material today for electro-optic modulator applications. Due to certain limitations of LiNbO<sub>3</sub>, such as its low electro-optic coefficient, an alternative material is in searched for the next generation optical devices. CBN is one of the potential candidates due to its high electro-optic coefficient of 130 pm/V.

### **1.5 Challenges for deposition and device application**

The advances in the fabrication technology have made it possible to integrate ferroelectric thin films with microelectronic components for electro-optic devices. A number of deposition

techniques have been used so far for high quality ferroelectric thin films such as chemical solution deposition (CSD), RF magnetron sputtering, metal organic chemical vapour deposition (MOCVD), molecular beam epitaxy (MBE), and pulsed laser deposition (PLD) [24-27]. Each individual deposition technique has its advantages and disadvantages and the choice of the deposition technique used depends on the application. High performance electro-optic devices require a low scattering loss and a high electro-optic coefficient. Single crystalline thin films or highly oriented polycrystalline thin films based devices may achieve such high performance. Hetero-epitaxial thin film growth or deposition over a lattice-matched substrate results in high quality thin films for device application.

Ferroelectric thin films annealed above 650°C show good piezoelectric and electro-optic properties, [28]. This high temperature is not suitable for many ferroelectric thin films when the goal is to direct integration onto integrated circuits. As an example, Al metallization is hardly possible at post annealing temperatures above 500 °C. So, it has to be carried out after the ferroelectric thin film processing. CMOS compatibility also requires annealing temperatures lower than 650°C. Other metal, such as Pt, is also not suitable for high temperature annealing.

As mentioned earlier there exist several techniques for thin film deposition, among them CSD is popular because using CSD technique thin film composition can be controlled precisely. It is also easy to use, and cost effective. Using CSD techniques, films are deposited mainly by spin-coating or dip-coating after that two-step annealing is carried out. Firstly, at 350° C to pyrolyze the organic content and secondly, at high temperature (more than 550° C) to crystallize the film. Thin films deposited by CSD technique may have residual porosity and polycrystallinity both of

which increase the scattering loss [29]. Thin films deposited by the improved CSD technique on a lattice matched MgO substrate show not only the strongest electro-optic pockels effect but also reasonably low propagation loss of about 4 dB/cm [30]. Ferroelectric thin films can be deposited using MOCVD and atomic layer deposition (ALD) systems as well. Slow deposition rate of ALD makes it unfit for industrial applications. Using this type of deposition systems, volatile metallic-organic precursors are evaporated and guided to a reaction chamber, where the chemical reaction takes place and a thin film is deposited onto the heated substrate. Sometimes it is hard to find stable, volatile precursors of some cationic species.

Well-known physical deposition techniques for ferroelectric thin films are sputtering and PLD. In PLD, a short wavelength, high power laser is focused on a target inside a vacuum chamber. The evaporated material is condensed onto a substrate. PLD has many advantages such as the stoichiometric transfer of material from a target to substrate, and relatively high deposition rates. In spite of these significant advantages, PLD is not suitable for industrial applications and only limited to the research environment. There are basically three main reasons for that: firstly, due to the forwarded direction of plasma plume the deposited film is non-uniform and composition can vary across the film. Secondly, the area of uniformly deposited material is also quite small, typically  $\sim 1\text{cm}^2$ . Finally, the ablated material contains macroscopic globules of molten material, called droplet. The deposition of these droplets at the substrate is obviously negative to the properties of the film being deposited [30].

The fabrication technologies for many ferroelectric materials have been studied so far. Every individual material has different challenges. One of the well-studied materials are Lead Zirconate

Titanate (PZT) based ferroelectrics. The problem of this material is the volatility of lead oxide. To overcome this problem 10~20% excess lead is added to the Pb precursors. Other Pb based ferroelectric materials like PSZT,  $\text{Pb}(\text{Mg},\text{Nb})\text{O}_3$  and  $\text{Pb}(\text{Sc},\text{Ta})\text{O}_3$  also have similar challenges.

Chemical compatibility of film and substrate is another key challenge for ferroelectric thin film growth. Difference in the thermal expansion coefficients and lattice mismatch limit the epitaxial growth of ferroelectric thin films. Even at low annealing temperature these thin films could show cracks which will deteriorate the film properties. Sometimes, it may require an intermediate buffer layer not only for diffusion barriers but also to release the thermal stress which promotes the epitaxial growth on ferroelectric films during the high temperature process. Since, an epitaxially grown buffer layer is required to obtain epitaxial films, the deposition process is mainly limited to single crystalline lattice matched substrates, such as MgO,  $\text{SrTiO}_3$ , and sapphire, etc. CBN was previously deposited on various substrates such as n: $\text{SrTiO}_3$ , MgO, etc. But, n: $\text{SrTiO}_3$  is not suitable for device application, whereas on MgO the electro-optic coefficient reduces significantly due to the lattice mismatch. In this work, CBN is optimized on lattice matched substrates based on deposition pressure and temperature which has discussed more details in chapter 3.

## **1.6 Structure of the thesis**

This thesis is organized in a step-by-step approach that leads to the CBN based grating coupler device on GGG. Apart from the first chapter which addresses context, objectives, and challenges of this work, the main contents of the thesis are structured as follow:

Chapter 2 give details about the deposition and fabrication techniques used for CBN thin film deposition and device fabrication. For CBN thin film deposition the PLD technique is used. XRD and XPS are used for structural and compositional analysis respectively. Surface properties are analysed by AFM and SEM. Optical transmission of CBN thin films are measured using ellipsometry.

Chapter 3 gives an overview of the structural and optical characteristics of the CBN thin film. Different issues related to substrate cleaning and the choice of substrate is addressed. The influences of a new substrate on the structural, crystallization, optical properties of the CBN thin film are studied. The details of the PLD technique for CBN thin film used in this work are presented. The importance of new substrate to grow highly oriented CBN thin films is studied in detail. The detailed optimization of the films in terms of the deposition temperature and pressure is presented. The influence of the processing parameters for the growth optimization of the ferroelectric thin films has been studied in detail. AFM, SEM analysis have been used to study the micro-structure and roughness of the thin films. X-ray diffraction and rocking curve measurements are used to study the crystallization and film quality under different deposition conditions. The SEM and AFM measurements confirm the smooth surface of the CBN thin film which is suitable for photonic applications.

In Chapter 4, the fabrication and characterization of CBN grating coupler is explained in detail. CBN films are patterned using an ICP reactive ion etching system and the etching process and other fabrication steps are explained in details. Then, the characterizations of the devices are explained. We are able to couple light in thin CBN based grating coupler. Finally, a summary of

the results from this research work and some potential future research directions in the improvement of CBN thin film deposition and device performance are described in Chapter 5.

## 1.7 References

1. Lei, X.Y., et al., “Dielectric, ferroelectric and piezoelectric properties of 100-oriented  $\text{Pb}_{0.4}\text{Sr}_{0.6}\text{TiO}_3$  thin film sputtered on  $\text{LaNiO}_3$  electrode”, *Journal of Crystal Growth*, 347, 1, (2012).
2. Kobayashi, T., et al., “Microelectromechanical systems-based electrostatic field sensor using  $\text{Pb}(\text{Zr},\text{Ti})\text{O}_3$  thin films”. *Japanese Journal of Applied Physics*, 47, 9S, (2008).
3. Kang, T.D., et al., “Large electro-optic effect in single-crystal  $\text{Pb}(\text{Zr},\text{Ti})\text{O}_3$  (001) measured by spectroscopic ellipsometry”, *Journal of Applied Physics*, 104, 9, (2008).
4. M. Eßer, et al., “Single Crystal Growth of the Tetragonal Tungsten Bronze  $\text{Ca}_x\text{Ba}_{1-x}\text{Nb}_2\text{O}_6$  ( $x = 0.28$ ; CBN-28)”, *Journal of Crystal Growth*, 240(1-2), 1–5, (2002).
5. S. Vigne, et al., “Structural and optical properties of  $\text{Ca}_x\text{Ba}_{1-x}\text{Nb}_2\text{O}_6$  thin films deposited by radio frequency magnetron sputtering”, *Optical Materials Express*, 5, 11, (2015).
6. Paul F. Ndione, et al., “Hybrid integration of  $\text{Ca}_{0.28}\text{Ba}_{0.72}\text{Nb}_2\text{O}_6$  thin film electro-optic waveguides with silica/silicon substrates”, *Optics Express*, 17, 17, (2009).
7. Stéphane Bancelin, et al., “Nonlinear optical properties of calcium barium niobate epitaxial thin films”, *Optics Express*, 24, 15, (2016).
8. Wooten, E.L., et al., “A review of lithium niobate modulators for fiber-optic communications systems”, *IEEE Journal of Selected Topics in Quantum Electronics*, 6, 1, (2000).
9. Springer Hand book of Electronic and Photonic Materials, S. Kasap, P. Capper, © Springer, USA, (2006).
10. Z. Yu, et al., “Ferroelectric-relaxor behavior of  $\text{Ba}(\text{Ti}_{0.7}\text{Zr}_{0.3})\text{O}_3$  ceramics”, *Journal of Applied Physics*, 92, 2655 (2002).

11. Panda, P.K. et al., “PZT to Lead Free Piezo Ceramics: A Review”, *Ferroelectrics*, 474, 1, (2015).
12. Bowen, C.R., et al., “Pyroelectric materials and devices for energy harvesting applications”, *Energy & Environmental Science*, 7, 12, (2014).
13. Bruchhaus, R., et al., “Optimized PZT thin films for pyroelectric IR detector arrays”, *Journal of Electroceramics*, 3, 2, (1999).
14. Damjanovic, et al., “Ferroelectric, dielectric and piezoelectric properties of ferroelectric thin films and ceramics”, *Reports on Progress in Physics*, 61, 9, (1998).
15. *Fundamentals of Photonics*, Bahaa E. A. Saleh, Malvin Carl Teich, Copyright © 1991 John Wiley & Sons, Inc.
16. M. Dawber, et al., “Physics of thin-film ferroelectric oxides”, *Reviews of Modern Physics*, 77, 1083, (2005).
17. Peng Gao, et al., “Organohalide lead perovskites for photovoltaic applications”, *Energy and Environmental Science*, 7, 2448, (2014).
18. Haitao Huang, “Solar energy: Ferroelectric photovoltaics”, *Nature Photonics* 4, 134 – 135, (2010).
19. Hong-Bo Chen, et al., “Electric field control of multiferroic domain wall motion”, *Journal of Applied Physics*, 115, 133913, (2014).
20. S. Y. Yang, et al., “Above-bandgap voltages from ferroelectric photovoltaic devices”, *Nature Nanotechnology*, 5, 143 – 147, (2010).
21. S. Y. Yang, et al., “Photovoltaic effects in BiFeO<sub>3</sub>”, *Applied Physics Letters*, 95, 6, (2009).
22. D. Cao, et al., “High-Efficiency Ferroelectric-Film Solar Cells with an n-type Cu<sub>2</sub>O Cathode Buffer Layer”, *Nano Letters*, 12, 2803, (2012).

23. Niu, G., et al., "Epitaxy of BaTiO<sub>3</sub> thin film on Si(001) using a SrTiO<sub>3</sub> buffer layer for non-volatile memory application", *Microelectronic Engineering*, 88, 7, (2011).
24. Cooney, et al., "Processing of sol-gel derived PZT coatings on non-planar substrates", *Journal of Micromechanics and Microengineering*, 6, 3, (1996).
25. Menou, N., et al., "(111)-oriented Pb(Zr,Ti)O<sub>3</sub> films deposited on SrRuO<sub>3</sub>/Pt electrodes: Reproducible preparation by metal organic chemical vapor deposition, top electrode influence, and reliability", *Journal of Applied Physics*, 102, 114105, (2007).
26. Abel, S., et al., "A strong electro-optically active lead-free ferroelectric integrated on silicon", *Nature Communications*, 4, 1-6, (2013).
27. Borowiak, A.S., et al., "Pulsed laser deposition of epitaxial ferroelectric Pb(Zr,Ti)O<sub>3</sub> films on silicon substrates", *Thin Solid Films*, 520, 14, (2012).
28. Paul F. Ndione, et al., "Structural and optical properties of epitaxial Ca<sub>x</sub>Ba<sub>1-x</sub>Nb<sub>2</sub>O<sub>6</sub> thin films grown on MgO by pulsed laser deposition", *Journal of Applied Physics*, 103, 033510 (2008).
29. Xu, Z.M., et al., "Monolithically integrated optical modulator based on polycrystalline Ba<sub>0.7</sub>Sr<sub>0.3</sub>TiO<sub>3</sub> thin films", *Applied Physics Letters*, 88, 16, (2006).
30. Petraru, A., et al., "Integrated optical Mach-Zehnder modulator based on polycrystalline BaTiO<sub>3</sub>", *Optics Letters*, 28, 24, (2003).

# Growth and Characterization Techniques of Thin Films

## 2.1 Growth techniques of thin films

There are many deposition techniques available for material formation. In principle, thin film deposition techniques are either purely chemical or physical. Examples for physical deposition technology and chemical deposition technology are evaporative methods and gas- and liquid-phase chemical processes respectively. Some deposition technologies are based on glow discharges and reactive sputtering; combining both physical and chemical reactions can be categorized as physical-chemical methods. For our experiment, we have used pulsed laser deposition which is a physical vapor deposition technique.

### 2.1.1 Pulsed Laser Deposition (PLD)

PLD is a physical vapor deposition technique which is one of the most versatile approaches to oxide thin film growth. PLD is now a widely used approach for film deposition even though significant development of this technique began only in the late 1980s. In this technique, a pulsed-laser is focused onto a target of the material to be deposited inside a vacuum chamber. The substrates, on which the film is grown, kept few centimeters away from the target. A schematic representation of PLD system is shown in figure 2.1. The detailed physical phenomena involved in the interaction of high-powered nanosecond excimer-laser pulses with bulk targets resulting in evaporation, plasma formation, and subsequent deposition of thin films is well described in reference [1].

In PLD, photonic energy is coupled to the bulk starting material via electronic processes. An intense laser pulse is introduced into a vacuum chamber through an optical window. The laser pulse is focused onto a solid or liquid surface known as “target”, where it is partially absorbed. Depending on the type of interaction of the laser beam with the target, the PLD process can be classified into three separate regimes: (i) interaction of the laser beam with the target material resulting in evaporation of the surface layers (ii) interaction of the evaporated material with the incident laser beam resulting in isothermal plasma formation and expansion, and (iii) anisotropic adiabatic expansion of the plasma leading to the characteristic nature of the laser deposition process [1]. Above a certain laser power, each pulse with sufficiently high laser energy density vaporizes or ablates a small amount of the material in the form of an ejected luminous plume. Certain threshold power density is required to produce such a plume which depends on the target material, its morphology, and the laser pulse wavelength and duration. The ablated materials are then ejected from the target in a forward directed plume and recondense on a substrate, where film growth occurs. The growth process may be supplemented by a passive or reactive gas or ion source, which may affect the ablation plume species in the gas phase or the surface reaction [2].

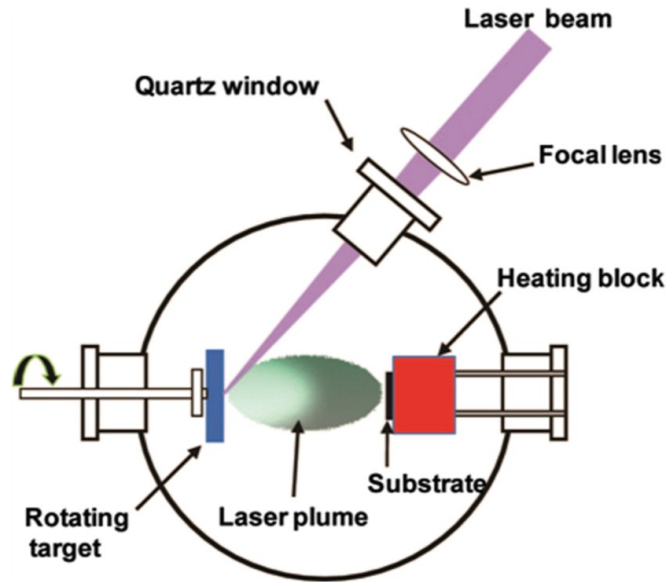


Figure 2.1: Schematic illustration of the pulsed laser deposition (PLD) setup [2].

The specified process involved with PLD has been widely investigated using not only for in-situ but also for ex-situ characterization tools for a number of systems. Stoichiometric transfer of ablated material from multi-cation targets for many materials arises from the non-equilibrium nature of the ablation process itself due to absorption of high laser energy density by a small volume of material. When the laser fluence is low it simply heats the target and thermal evaporation of the target species occur. With the increase of laser fluence, an ablation threshold is reached where laser energy absorption is higher than that needed for evaporation [3]. The ablation threshold is dependent on the absorption coefficient of the material. At higher laser fluencies, absorption by the ablated species occurs and plasma at the target surface is formed. A background gas is often introduced inside the vacuum chamber which serves two purposes. Firstly, an oxide thin film formation requires an oxidizing species as a component of flux. The amount of oxygen required for phase formation will depend on the thermodynamic stability of the desired oxide phase [4-5]. In addition to actively participating in the chemistry of oxide

growth, the background gas also reduce the kinetic energies of the ablated species. The kinetic energies can be in the order of several 100 eV which are sufficiently high to create defects in the growing film. This high kinetic energy can be reduced to less than 1 eV with the help of background gas due to the collision with gas molecules. Substrate temperature is another important parameter for optimizing the film. Substrate temperature influence nucleation processes and the mobility of the deposit across the substrate. Besides temperature and background gas, material distribution depends on laser–target interaction, laser peak fluence, intensity profile, laser spot aspect ratio, and physical properties of the target [6].

Pulsed-laser deposition has several attractive features, including stoichiometric transfer of material from the target, generation of energetic species, hypothermal reaction between the ablated cations and molecular oxygen in the ablation plasma, and compatibility with background pressures ranging from UHV to 100 Pa [7]. With appropriate deposition conditions, epitaxial oxide thin film can be deposited either with stoichiometric targets of the material of interest or with multiple targets for each element. Beside this, PLD also has some other key advantages, such as, the energy source being outside the vacuum chamber which provides a much greater degree of flexibility in material usage and geometrical arrangements, film growth rate can be controlled at atomic level, source material is evaporated only to the area defined by the laser focus, the ratios of the elemental components of the bulk and thin film remain same under optimal condition, and almost any condensed matter material can be ablated, etc.

While having many advantages, PLD also has some limitations. Firstly, PLD is not suitable for industrial applications where large area substrates need to be effectively coated within a

reasonable time. Secondly, the thickness distribution of the synthesized film from a stationary plume is quite non-uniform due to the highly forward-directed nature of the ablation plume [6]. The dynamics of the laser ablation process results in a highly focused plume results in a significant variation in deposition rate over distances on the order of a few centimeters. For uniform film thickness over large areas, one can combine substrate rotation with raster scanning of the ablation beam over a large ablation target. Thirdly, the ejection of micron sized particles in ablation process. These large particles create problems in the formation of multilayer device structures. Highly dense ablation target might reduce particles but not eliminate completely. Several techniques such as, off-axis laser deposition, line-of-sight shadow masks, and approaches that prevent the particles from reaching the substrate surface include velocity filters, etc. In addition, another interesting approach is to use two laser beams focused on separate targets situated perpendicular to each other [3]. The two ablation plumes collide with each other and form a new stream containing light plume components and almost no droplets. In this work we have deposited CBN using PLD and detailed is described in chapter 3.

## **2.2 Characterization Methods**

Various thin film characterization technologies are available and they are used depending on what kinds of information are required to be extracted from the thin film. To check the sample's surface on macroscopic, microscopic and atomic scale, optical microscopy, scanning electron microscopy, transmission electron microscopy, and scanning probe microscopies (such as scanning tunneling microscopy, atomic force microscopy etc) are used. X-ray diffraction measurements provide the information of sample's internal structure. To know the elemental composition, impurities, chemical states various techniques such as auger electron spectroscopy,

energy dispersive analysis of x-rays, x-ray photoelectron spectroscopy, secondary ion mass spectrometry, and rutherford backscattering are used. Ellipsometry measurements provide information about refractive index, and absorption dielectric properties, as a function of wavelength.

### 2.2.1 X-ray Diffraction (XRD)

In 1905, Albert Einstein introduced the photon concept [8]. In 1914, two English physicists, Sir William Henry Bragg and Sir William Lawrence Bragg had shown that the scattering of x-rays could be as “reflection” by successive planes of atoms within a crystal. It is also shown that when monochromatic X-ray passes through a periodic arrangement of atoms in a crystal it leads to the diffraction of the X-rays. Depending on the type of interference the intensity of the diffracted wave varied. In general, constructive interference of scattered photons leads to high intensity. Figure 2.2 shows the working principle of XRD where the wavelength of a monochromatic X-ray source ( $\lambda$ ), the diffraction angle ( $\theta$ ), and the distance between two parallel planes of periodically arranged planes ( $d$ ) are correlated by Bragg’s law as:

$$n\lambda = 2d\sin\theta$$

where  $n$  is the order of reflection.

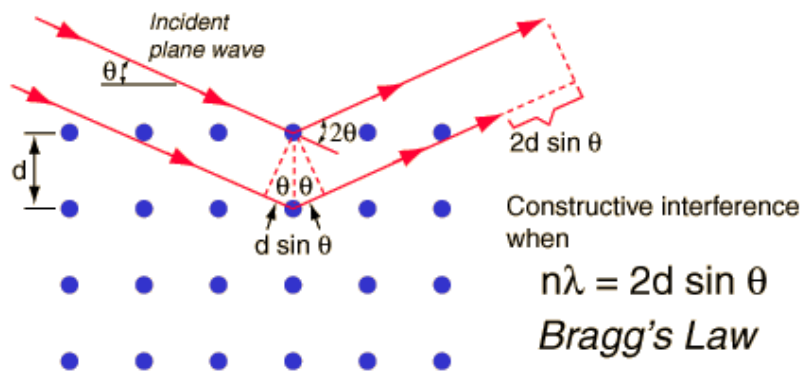


Figure 2.2: X-rays diffraction through a periodic arrangement of planes of atoms [9].

XRD is a powerful technique to measure crystal quality of a material since the X-ray wavelength ( $\lambda$ ) is almost equal to the distance of two atoms. A beam of X-rays from a monochromatic source is focused on the measuring sample which is fixed on a moveable flat plate. A detector gathers the diffracted beam from the sample. The diffracted beam from the sample is then detected, processed and counted which gives a signal proportional to the number of photons along the sample-detector direction. All possible diffraction directions of the lattice are obtained by scanning the sample through a range of  $2\theta$  angles. The signals are then plotted as a function of  $2\theta$  angles. A unique diffracted pattern is found for each parallel set of crystal planes. This pattern is then compared with standard library patterns (*X'Pert High Score*) to identify the measured materials. XRD measurements can extract information about a material such as lattice parameter, crystalline structure, and crystallite size distribution. For our measurements, we have used a high quality XRD system, namely the High resolution PANalyticalX'Pert Pro MRD 4-circle diffractometer system. With this system we can measure grazing incidence, Phi scan, phase analysis in  $\theta$ - $2\theta$  (Bragg-Brentano), high resolution reciprocal space mapping, texture analysis, high resolution rocking curve measurement, X-ray reflectivity, and residual stress analysis. In our study, we have mainly used  $\theta$ - $2\theta$  measurement to understand the structure and quality of the deposited film by PLD.

### **2.2.2 Atomic Force Microscopy (AFM)**

AFM is an important imaging technique for nanoscience which is used to determine topography and other surface properties. Similar to other scanning probe microscopes, the AFM raster scans a sharp probe over the sample to obtain information about the sample's surface with the changes in force between the probe tip and the sample. AFM provides various kinds of information about

the sample such as physical topography, as well as material's physical, magnetic, or chemical properties [12]. Figure 2.3 shows the working mechanism of AFM. A cantilever with a sharp probe tip is placed just above the sample surface. The force is dominated by the separation between the sample and probe tip and it is measured by the bending of the cantilever with an optical lever technique. A laser beam is focused on the back of probe tip and reflected into a photodetector. Forces between the tip and sample will create deflection of the laser in the photodetector. The tip is moved across the surface and the changes in force as a function of position are recorded to get surface topography and other properties.

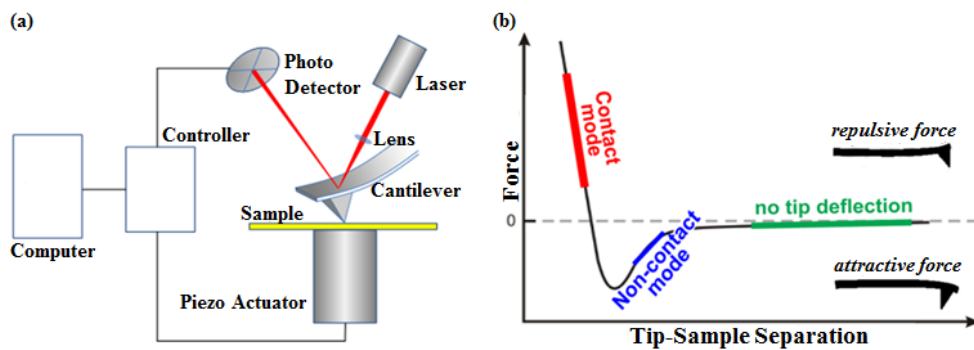


Figure 2.3: (a) Schematic representation of the AFM [10] (b) Force regimes governing the AFM measurement [11]

Generally, AFM imaging has 3 modes of operation: contact mode, tapping mode and noncontact mode. Figure 2.3 (b) shows a force vs distance curve indicating the three modes of operation. Contact mode is the most commonly used AFM imaging technique to get 3D topographical information on nanostructures and surfaces. “Contact” denotes the repulsive regime of the inter-molecular force curve, the part of the curve above the x-axis as shown in Figure 2.3 (b). As the name suggests, the tip and sample makes a soft physical contact with the sample while scans

over the sample surface by maintaining either a constant small height (less than a few angstrom) or under a constant force (van der Waals force, capillary force and force extracted by the cantilever itself). The main drawback of this mode of AFM is the tip remaining in contact with the sample and large lateral forces can be exerted when the tip is dragged over it. These large forces may damage the samples and provide deformed images. Tapping mode is another mode of operation for AFM. In tapping mode the tip makes intermittent contact with the surface [12]. The cantilever is driven at its resonant frequency and the tip touches the scanning surface only for a fraction of its oscillating period. Since the tip touches the sample for a small fraction of its oscillation period, the lateral forces are reduced dramatically. Though tapping mode operation is slower than contact mode, it can provide higher lateral resolution (1~5 nm). Tapping mode is more useful for the samples that are weakly bound to the surface or samples that are soft (polymers, thin films). In non-contact mode of operation the cantilever oscillate above the sample's surface at distance (approximately at least one nanometer) such that it is not in the repulsive regime but in the attractive regime of the inter-molecular force curve. The operation of non-contact imaging is quite difficult in ambient conditions because as the tip is brought close to the surface, a small capillary bridge between the tip and the sample causes the tip to “jump-to-contact” [12]. This method is useful for soft samples but yields lower lateral resolution due to tip-sample separation.

The choice of AFM mode mainly depends on the surface characteristics of interest and on the hardness/stickiness of the sample. In our experiments, we used AFM to investigate surface characteristics of as grown thin films using a Veeco DI-EnviroScope microscope (Veeco Instruments, Inc.). We have chosen tapping as a preferred mode for imaging of surface

topography. In our work, we have used AFM for the surface roughness analysis of CBN and details is described in chapter 3.

### **2.2.3 Scanning Electron Microscopy (SEM)**

SEM is a technique for high-resolution imaging of objects. Similar as optical microscope which uses visible light, SEM uses electrons for imaging. The advantages of SEM over a regular light, or optical, microscope include much higher magnification of objects at upward of 300,000 times the size of the object studied and greater depth of field up to 100 times [13-14]. These numbers are known as magnification power.

The SEM generates a beam of electrons to the specimen inside the vacuum chamber. The electrons are created either by a field emission cathode or a thermal emission source, such as a heated tungsten filament. Typical beam diameter of the SEM is between 5 nm to 2  $\mu\text{m}$  and the accelerating voltage is from 2 to 50 kV. The energy of the incident electrons can be as low as 100 eV or as high as 30 keV. An anode is placed just below the electron gun and negatively charged electrons are attracted by positively charged anode and so they are headed toward that direction. A series of lenses are used to focus the beam towards the specimen. The lenses are made of magnets capable of bending the path of electrons. By doing so, the lenses focus and control the electron beam, ensuring that the electrons end up precisely where they need to go [14]. Scanning coils near the end of the column direct and position the focused beam onto the sample surface. The electron beam is scanned over the surface in a raster pattern for imaging. Figure 2.4 shows the schematic representation of a SEM system. SEMs operate under vacuum

condition because without a vacuum chamber the electron beam generated by the electron gun would encounter constant interference from air particles in the atmosphere.

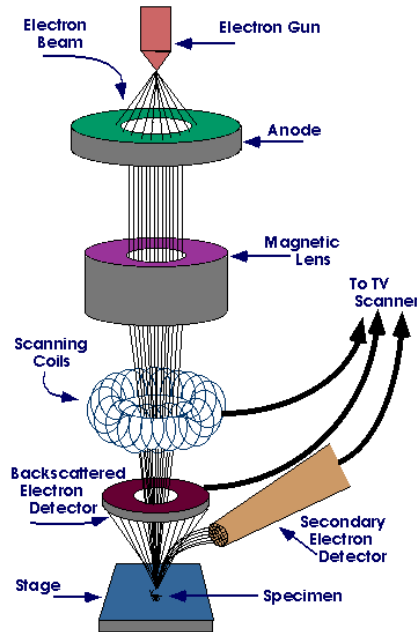


Figure 2.4: Schematic representation of SEM [15]

In SEM two types of signals, secondary and backscattered electrons are utilized for visual inspection. Secondary and backscattered electrons are constantly being produced within the specimen's surface and near-surface material while under the electron beam due to elastic and inelastic scattering. Secondary electrons are a result of the inelastic collision of incident electrons with specimen electrons. They are generally characterized by possessing energies of less than 50 eV [15]. Imaging with secondary electrons provides information about morphology and surface topography with a resolution of  $\sim 10$  nm or better [16]. Scintillator type detectors (Everhart-Thornley) are used for secondary electron imaging. This detector is charged with a positive voltage to attract electrons to the detector for improved signal to noise ratio [14].

High-energy electrons that are ejected by an elastic interaction between incident electrons and specimen nuclei or electrons are referred to as backscattered electrons. The energy of backscattered electrons is more than 50 eV [17]. Detectors for backscattered electrons can be scintillator types or a solid-state detector. Another type of signal that is used for scanning electron microscopy is the x-ray signal. The x-ray signal is a result of recombination between free electrons and holes that are generated within the material. Backscattered electron detectors and X-ray detectors, can provide the compositional information of a substance. An SEM image is created by scanning the incident electron beam in a raster pattern across the desired scan area. The emitted electrons are detected for each particular position in the scan area of the specimen by an appropriate detector. The intensity of the emitted electron signal is displayed in the scale of brightness which represents the morphology of the sample surface area on a display monitor and/or in a digital image file. High-resolution imaging is performed with the chamber at higher vacuum, typically from  $10^{-5}$  to  $10^{-7}$  Torr.

One of the key limitations of SEM is that it cannot detect electrically insulating specimens so an electrically conductive coating must be applied to it for study in conventional SEM's, unless the instrument is capable of operation in a low vacuum mode. In our work, we have used SEM for the surface roughness analysis of CBN and details is described in chapter 3.

#### **2.2.4 Energy Dispersive X-Ray Spectroscopy (EDS or EDX)**

EDS is a nondestructive localized chemical analysis technique used in conjunction with SEM. In principle, all elements from atomic number 4 (Be) to 92 (U) can be detected, though not all

instruments are equipped for 'light' elements detection [18]. When a beam of electron interacts with target sample it produces a variety of emission, including X-ray. The EDS technique detects x-rays emitted from the sample to identify what those particular elements are and their relative proportions (atomic % for example) of the analyzed volume. EDS can be used to find the chemical composition of materials down to a spot size of 1  $\mu\text{m}$  or less [18].

When the sample is bombarded by the SEM's electron beam, it leaves thousands of the sample atoms with holes in the electron shells where the secondary electrons used to be. The atoms are in unstable state due to the “holes” in inner shells. To stabilize the atoms, electrons from outer shells will drop into the inner shells. Since the outer shells are at higher energy state, an x-ray is emitted to balance the energy difference between the two electrons' states [19]. Figure 2.5 shows EDS Spectrum for Alloy MP35N [18].

The characteristic X-ray lines are named according to the shell in which the initial vacancy occurs and the shell from which an electron drops to fill that vacancy [20]. For instance, if the initial vacancy occurs in the K shell and the vacancy filling electron drops from the adjacent (L) shell, a  $K\alpha$  x-ray is emitted. If the electron drops from the M shell then  $K\beta$  x-ray is emitted. Similarly, if an L-shell electron is ejected and an electron from the M-shell fills the vacancy,  $L\alpha$  radiation will be emitted.

Elements having lower atomic number have fewer filled shells, they have fewer X-ray peaks. As an example, Carbon has only one peak, a  $K\alpha$  X-ray at 282 eV. On the other hand, the higher atomic numbered elements shows more numbers of X-ray peaks than lower atomic numbered

elements. While some of the high atomic numbered X-rays can be over 50 keV, a spectral range of 0-20 keV can detect all the elements from boron to uranium [20].

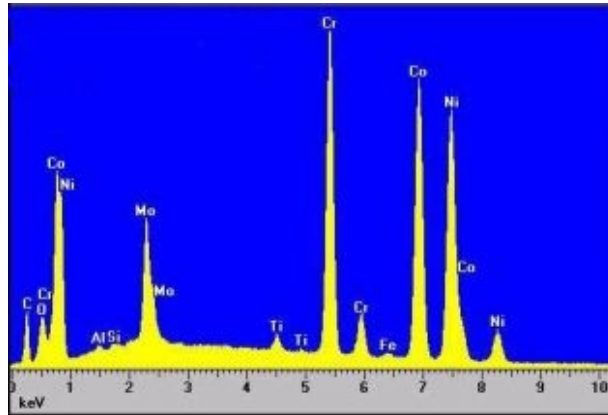


Figure 2.5: EDS Spectrum for Alloy MP35N [15]

The EDS x-ray detector measures the relative abundance of emitted x-rays versus their energy. The detector is typically a lithium-drifted silicon, solid-state device. When an incident x-ray strikes the detector, it creates a charge pulse that is proportional to the energy of the x-ray. The charge pulse is converted to a voltage pulse by a charge-sensitive preamplifier. The signal is then sent to a multichannel analyzer, where the pulses are sorted by voltage. The energy, as determined from the voltage measurement, for each incident x-ray is sent to a computer for display where the spectrum of x-ray energy versus counts is evaluated to determine the elemental composition of the sampled volume [18].

Qualitative and quantitative analysis are performed in EDS measurement. The objective of qualitative analysis is to identify the elements present in the sample and is a prerequisite for quantitative analysis. The sample x-ray energy values from the EDS spectrum are compared with

known characteristic x-ray energy values to find out the presence of an element in the sample. Usually, elements with atomic numbers ranging from that of Beryllium to Uranium can be detected. Depending on the element and the sample matrix, the minimum detection limits vary from approximately 0.1 to a few atom percent. The identification of the lines in the spectrum is done through qualitative analysis and is fairly straightforward owing to the simplicity of X-ray spectra.

X-rays generated by emission from different energy-level shells (K, L and M) in different elements can have overlapping energy peaks. In such situation it is very difficult to distinguish different element peaks appropriately. At higher energies individual peaks may correspond several different elements, in this case, deconvolution methods can be used for peak separation [21]. Furthermore, EDS cannot detect the lightest elements, typically below the atomic number of Na for detectors equipped with a Be window also samples must be compatible with a moderate vacuum atmosphere. In our work, we have used EDS to find the chemical composition of CBN target.

### **2.2.5 X-Ray Photoelectron Spectroscopy (XPS):**

X-ray Photoelectron Spectroscopy (XPS), also known as Electron Spectroscopy for Chemical Analysis (ESCA), is the most widely used surface analysis technique because it can be applied to a broad range of materials and provides valuable quantitative and chemical state information from the surface of the material being studied [22]. The average depth of analysis for an XPS measurement is approximately 5 ~ 7 nm.

The X-ray excites the electrons of the sample atoms, and if their binding energy is lower than the X-ray energy, they will be emitted from the parent atom as a photoelectron. The energy and intensity of the emitted photoelectrons are analysed to identify and determine the concentrations of the elements present. These photoelectrons originate from a depth of <10 nm therefore the information obtained is from within this depth.

The sample is placed in an ultrahigh vacuum environment and irradiates the sample surface with a low-energy, monochromatic x-ray source. The incident x-rays hit and transfer energy to a core-level electron, and it is emitted from its initial state of sample atoms with a kinetic energy depending on the incident x-ray and binding energy of the atomic orbital from which it originated. The energy of a photo-emitted core electron is a function of its binding energy and is characteristic of the element from which it was emitted. Energy analysis of the emitted photoelectrons is the primary data used for XPS and basically characterizes the element and configure the electrons inside the atom such as 1s, 2s, 2p, 3s etc. When the core electron is ejected by the incident x-ray, an outer electron drops-off and fills the core hole. The energy of this transition is balanced by the emission of an Auger electron or a characteristic x-ray. In addition to emitted photoelectrons, analysis of Auger electrons is also used in XPS.

An electron energy analyzer is used to detect the photoelectrons and Auger electrons emitted from the sample also their energy is determined as a function of their velocity entering the detector. A surface composition spectrum is obtained by counting the number of photoelectrons and Auger electrons as a function of their energy. The energy corresponding to each peak represents the existence of the element in the sampled volume. The area under a peak in the

spectrum is a measure of the relative amount of the element represented by that particular peak. The peak shape and precise position indicate the chemical state for the element.

XPS is a surface sensitive technique because only those electrons generated near the surface escape and are detected. The photoelectrons of interest have relatively low kinetic energy. Due to inelastic collisions within the sample's atomic structure, photoelectrons originating more than 20 to 50 Å below the surface cannot escape with sufficient energy to be detected [23]. The importance of surface engineering increases with the demand for high performance materials. The physical and chemical interactions that occur at the surface or at the interfaces of a material provide important information about the materials. Measurements such as survey scan, high resolution multiplex scan, quantization, depth profile, and mapping provide key analytical information about any materials. In survey scan, energy peaks of the uppermost 20~50 Å of the analyzed surface give the information of elemental composition. Most of the elements, except hydrogen and helium, can be detected with detection limits approximately 0.1 atom percent. The high resolution multiplex scan evaluates the chemical state(s) of each element through its core electron binding energies. With the quantization technique, concentrations of the elements are determined in the survey scan by integrating the area under a characteristic peak for each element.

A depth profile of the sample can be obtained by combining a sequence of ion gun etch cycles interleaved with XPS measurements from the current surface. An ion gun is used to etch the material for a period of time. Each ion gun etch cycle exposes a new surface and the XPS spectra provide the composition of these surfaces. The actual depth for each XPS analysis is dependent

on the etch-rate of the ion-gun. The relative concentration of one or more elements can be obtained as a function of lateral positions on the sample surface with the mapping technique.

XPS has a wide range of application such as surface analysis of organic and inorganic materials, determining composition and chemical state information from surfaces, thin film oxide thickness measurements, depth profiling for thin film composition, analysis of thin film contamination, and evaluation of adhesion failures, etc. In our work, we have used XPS for the chemical compositional analysis of CBN thin film. More details of XPS analysis of CBN thin film is found in chapter 3.

### **2.3 Electron-beam lithography**

Electron-beam lithography often called e-beam lithography is the tool used in nanofabrication to draw custom shapes on substrate covered with electron-sensitive resist. The beam of electron changes the solubility of the resist which can be removed selectively depending on the types of the resist and exposed or non-exposed regions by rinsing in developer. The major advantage of e-beam lithography over photolithography is that it can create small structures in the resist. E-beam lithography can draw custom patterns with sub-10 nm resolution. Figure 2.6 shows a resist patterning by ebeam.

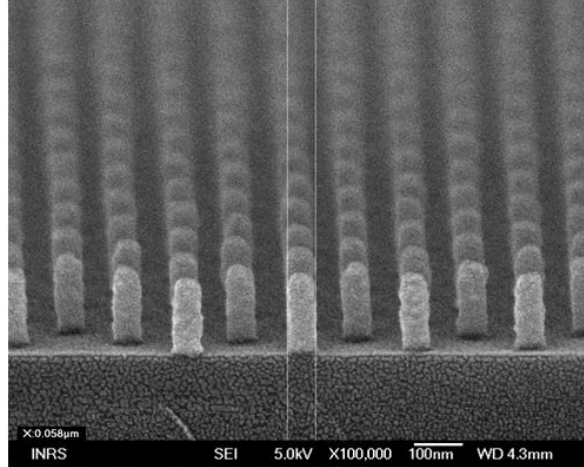


Figure 2.6: 60nm width posts of negative ebeam resist (maN2403) [25]

Key components of electron-beam lithography are electron sources, lenses, stage, stitching and alignment. The minimum time to expose a given area is defined by the following formula [23]:

$$DA=TI$$

where  $D$  is the dose,  $A$  is the area exposed,  $T$  is the time to expose, and  $I$  is the beam current. E-beam lithography is not suitable for industrial applications because of its limited throughput. An optical maskless lithography is much faster than e-beam lithography for the same resolution photomask patterning. Main application for e-beam lithography is photomask fabrication, low-volume production of semiconductor devices, and in research and development. In our experiment, we have used ebeam writer VB6 UHR EWF for grating coupler fabrication which is discussed in chapter 4.

## 2.4 Inductively Coupled Plasma (ICP) Etcher

Inductively Coupled Plasma (ICP) refers to a system configuration where plasma is generated by means of inductively coupling RF power in the source while independently controlling the ion energy bombarding the substrate via the applied bias power [24]. This independent control

allows for a wider process space to address a range of requirements from chemical processes such as the etching of Si or Cr to the physical processes such as the etching of sapphire. Plasma generation is done using 2 MHz RF power in the source while the bias is applied using 13.56 MHz RF power [25]. As shown in figure 2.7 the top portion of the reactor correspond to ICP part where a coil is surrounded by a dielectric material usually Alumina [26]. ICP has a 380 mm high density plasma source which can provide a 2 MHz RF signal and can be extended up to 5 kW. The diameter of lower electrode is 240 mm by which a substrate up to 6 inches can be used and etching homogeneity can be achieved typically 5%.

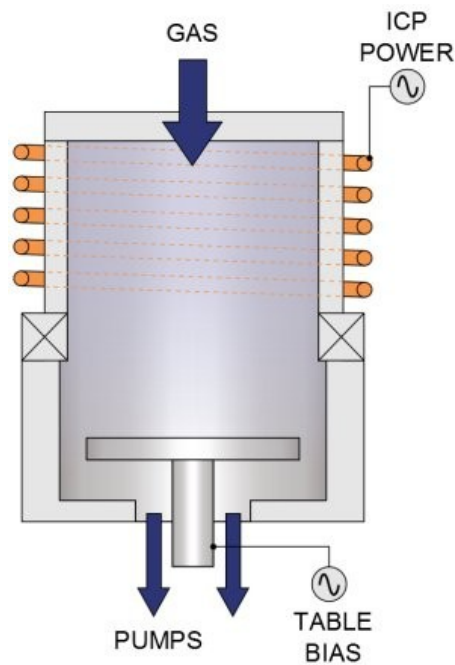


Figure 2.7: Inductively Coupled Plasma (ICP) Etching System [26]

When a RF signal of 13.56 MHz is applied to the lower electrode the generator can provide up to 600 W. The tray height can be controlled according to the need. In our experiment we have used 35 mm from the bottom of the system during etching. Substrate temperature can be controlled in the range of -150 °C and +400 °C with the help of liquid nitrogen and heating system. Thermal

contact between sample and substrate is maintained with helium. Required etching gases are introduced by controlling their flow in the range of 1-100 sccm and the total pressure of the chamber is controlled in real time by opening of pumping valve. Figure 2.8 (a) shows  $\text{SiO}_2$  etching with our fluorine ICP etcher whereas figure (b) shows GaAs etching by chlorine ICP etcher. The etching depth was monitored in real time by a laser interferometry system. This technique relies on measuring the optical reflection of the etching material. A laser beam at 675 nm is sent to the surface of the sample and the reflection beam is collected on a detector. A laser beam at 675 nm is sent quasi-orthogonally to the surface of the sample and the reflected beam is collected on a detector. The evolution of the reflection is then studied according to the type of material to be etched.

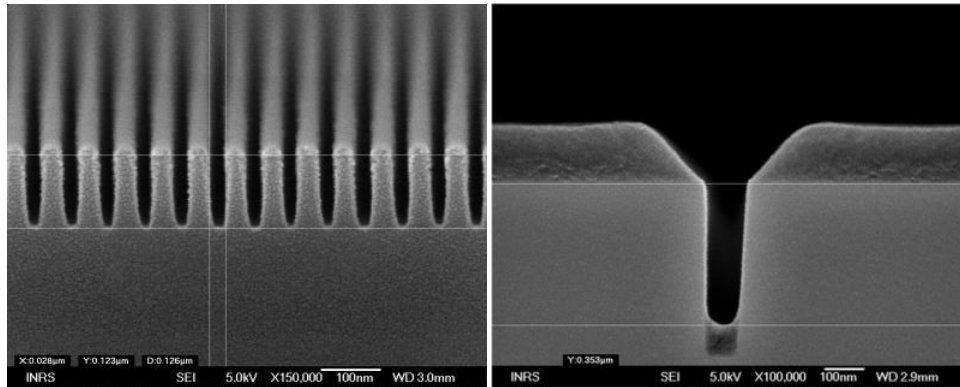


Figure 2.8: (a). Nanometric-anisotropic etching of  $\text{SiO}_2$  (30nm lines and spaces grating) for Nanoimprint applications, (b). Anisotropic etching of GaAs (80nm width trenches, resist mask still in place) [25].

The experiments were carried out in Oxford Instruments ICP-RIE reactors (PlasmaLab System 100) at the INRS. More details about the etching procedure is described in chapter 4.

## 2.5 Comparison of the characterization techniques

A comparison of all presented characterization techniques have been summarized in the bellow table.

**Table 2-1:** comparison of all presented characterization techniques

Name of the Technique	Functions	Limitations
<b>PLD</b>	Thin film deposition	Characterization not possible.
<b>XRD</b>	Structural characterization	Surface morphology cannot be measured.
<b>AFM</b>	Surface morphology measurement	Cannot do structural characterization
<b>SEM</b>	Surface morphology measurement	Cannot do structural characterization
<b>EDS</b>	Atomic % measurement	Not precise for thin film.
<b>XPS</b>	Chemical composition measurement	Cannot do structural characterization
<b>Electron-beam lithography</b>	Device patterning	Slow process
<b>ICP Etcher</b>	Thin film etching	-

## 2.6 Conclusion

In this chapter we have described the principle of all the experimental techniques that we have used in our study. All these experimental techniques are available at INRS and we have used them for our experiments.

## 2.7 References

1. Rajiv K. Singh, et al., "Pulsed-laser evaporation technique for deposition of thin films: Physics and theoretical model", *Physical Review B*, 41, 8843, (1990).
2. Willmott, et al., "Pulsed laser vaporization and deposition", *Reviews of Modern Physics*, 72, 315, (2000).
3. *Pulsed Laser Deposition of Thin Films: Applications-Led Growth of Functional Materials*, Robert Eason, Copyright © 1991 John Wiley & Sons, Inc..
4. Heungsoo Kim, et al., "Laser materials processing for micropower source applications: a review", *Journal of Photonics for Energy*, 4, 1, (2014).
5. Norton P. D., "Synthesis and properties of epitaxial electronic oxide thin-film materials", *Materials Science and Engineering R*, 43, 139, (2004).
6. J.T. Cheung, et al., *CRC Critical Reviews, Solid State Material Science*. 15, 63-109, (1988).
7. Einstein A. "Über einen die Erzeugung und Verwandlung des Lichtes betreffenden heuristischen Gesichtspunkt", *Annalen der Physik* 322, 6, (1905).
8. <http://hyperphysics.phy-astr.gsu.edu/hbase/quantum/bragg.html>
9. [http://www.qilerongrong.org/pic/AFM\\_principle.png](http://www.qilerongrong.org/pic/AFM_principle.png)
10. <http://www.intechopen.com/source/html/42103/media/image2.png>
11. *Scanning Probe Microscopy and Spectroscopy*, R. Wiesendanger, Copyright © 1994 Cambridge: Cambridge University Press.
12. <http://science.howstuffworks.com/scanning-electron-microscope.htm>
13. <http://www.mee-inc.com/hamm/scanning-electron-microscopy-sem/>
14. <https://www.purdue.edu/ehps/rem/rs/sem.htm>

15. Scanning Electron Microscopy: A Student's Handbook, M.T. Postek, K.S. Howard, A.H. Johnson and K.L. McMichael, (Ladd Research Ind., Inc. Williston, VT., 1980).
16. Geoffrey E. Lloyd, "Atomic number and crystallographic contrast images with the SEM: a review of backscattered electron techniques." Mineralogical Magazine, 51, 3-19, (1987).
17. <http://www.mee-inc.com/hamm/energy-dispersive-x-ray-spectroscopyeds/>
18. <http://www.microscopy.ethz.ch/aed.htm>
19. X-ray and image analysis in electron microscopy, 2nd Edition, John J. Friel, ©2003 Princeton Gamma-Tech.
20. [http://serc.carleton.edu/research\\_education/geochemsheets/eds.html](http://serc.carleton.edu/research_education/geochemsheets/eds.html)
21. <https://www.phis.com/surface-analysis-techniques/xps-esca.html>
22. <http://www.mee-inc.com/hamm/x-ray-photoelectron-spectroscopy-xps/>
23. Parker, N. W., et al., "High-throughput NGL electron-beam direct-write lithography system". SPIE Proceedings, 3997, (2000).
24. <http://www.plasma-therm.com/etch-icp.html>
25. <http://lmn.emt.inrs.ca/>
26. <https://www.oxford-instruments.com/OxfordInstruments/media/plasma-technology/Process%20Techniques/Content%20Small/ICP-Etching.jpg>

## Chapter 03

### CBN Thin Film Deposition and Optimization

#### 3.1 Substrate choice

The choice of a suitable substrate is crucial not only to grow an epitaxial thin film but also for device fabrication. For the epitaxial thin film deposition, the substrate should have a similar or nearly similar lattice parameter to that of the material to be deposited. Next criteria for choosing a suitable substrate should be thermal expansion coefficient, especially for material deposition at high temperature. Other parameters such as density, dielectric constant, refractive index, melting point, strain, and compatibility with silicon integration is also important for device fabrication. Table 3-1 shows the comparison of three different types of substrate with respect to CBN. To measure the electro-optic coefficient CBN was deposited on niobium doped strontium titanium oxide (Nb:STO) which also served as bottom electrode for the samples under investigation [5]. The electro-optic coefficient of the epitaxial CBN-28 on Nb:STO is reported 130 pm/V. Nb:STO is not a choice of substrate for device application because its refractive index is higher than that of CBN. Also, an epitaxial CBN thin film has already been deposited on magnesium oxide (MgO) single crystal substrate [1]. On MgO substrate, good CBN etching and excellent device fabrication is possible [2] but the electro-optic coefficient of CBN is reduced due to the lattice mismatch between them. Also, good waveguide has been demonstrated using CBN thin film deposited on MgO substrate [3-4]. It was certain that there will be good device on MgO but finally it was found that electro-optic coefficient of CBN thin film on MgO is very low. In spite of having such good structural and optical properties MgO is not a choice of substrate for device

applications because MgO is non-conducting so it is hard to verify the electro-optic coefficient of CBN thin film. Additionally, for the integration with Si, a thin buffer layer of MgO was also used to grow epitaxial CBN. But the MgO buffer layer shows lots of droplet and CBN thin film cracked after deposition. Beside these, both MgO and STO have large lattice mismatch with CBN which is not suitable to have high quality thin film for device applications. To overcome all these limitations, Gadolinium Gallium Garnet ( $Gd_3Ga_5O_{12}$ , GGG) is chosen as a suitable substrate for CBN thin film deposition for several reasons such as: direct lattice matching with CBN, lower thermal expansion coefficient compared to MgO or STO, lower refractive index than CBN, suitable for electro-optic measurement due to the possibility of finding conducting doped GGG, suitable for the integration with Si [6], and lower strain in compared to MgO or STO at growth and room temperature, etc.

**Table 3-1:** Comparison of different substrates for CBN deposition [P. F. Ndione and S. Vigne's PhD Thesis]

	<b>CBN</b>	<b>STO</b>	<b>MgO</b>	<b>GGG</b>
Structure	Tetragonal	Cubic	Cubic	Cubic
Lattice constant, a ( $\text{\AA}$ )	12.449	3.905	4.209	12.376
Density ( $\text{g/cm}^3$ )	5.1	5.12	3.58	7.09
Dielectric constant	156	300	9.8	30
Thermal expansion coefficient ( $10^{-6}/\text{K}$ )	12.5	10.3	12.8	8.2
Refractive index @ 1550 nm	2.22	2.37	1.72	1.95

Melting point ( °C)	-	2080	2852	1800
Type of lattice matching to CBN	-	Domain(3:1)	Domain(3:1)	Direct (1:1)
Strain @ room temperature	-	5.8% C	1.6% T	0.5% C
Strain @ growth temperature (750 °C)	-	4.5% C	3.1% T	0.7% C
Suitable for direct EO measurement?	-	Yes	No	Yes
Suitable for device fabrication?	-	No	Yes	Yes
Suitable for Silicon integration?	-	No	Yes	Yes
Available on bigger substrate?	-	1" x 1"	1" x 1"	4" diameter

### 3.2 Sample cleaning

Clean sample is the prerequisite to have smooth thin film. For our experiment, GGG samples were first cleaned in acetone with ultrasonic agitation for 15 minutes. In the next step, samples were cleaned in iso-propanol in an ultrasonic bath for 15 minutes, followed by cleaning in buffered oxide etch solution for 30 seconds and then the final cleaning in running deionised (DI) water. Finally, the samples are dried in an oven at 1000°C for 1 hour, before proceeding to the ferroelectric thin film deposition. The effect of substrate cleaning is clearly seen from the figure 3.1 and figure 3.2.

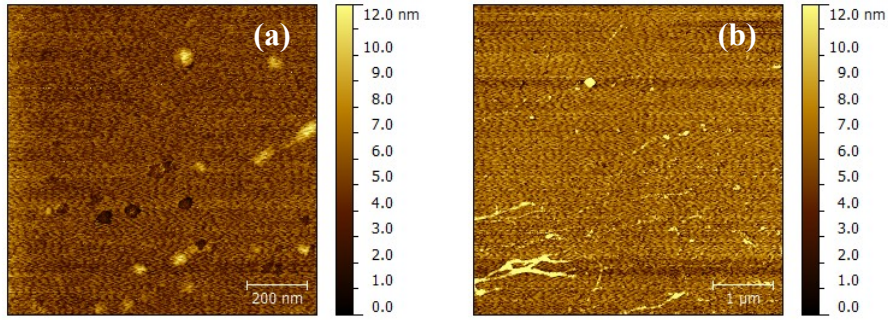


Figure 3.1: AFM images of GGG substrates cleaned by acetone and IPA. Scan area (a) 1  $\mu\text{m}$  and (b) 5  $\mu\text{m}$

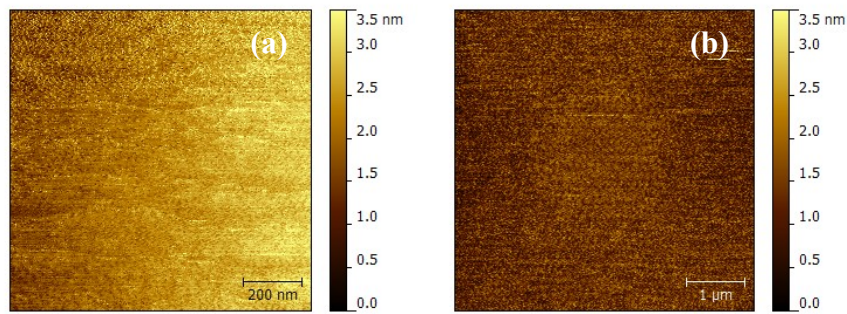


Figure 3.2: AFM images of GGG substrates cleaned by acetone, IPA, buffered oxide etch (BOE) cleaning. Images are taken after 1000°C annealing in oven. Scan area (a) 1  $\mu\text{m}$  and (b) 5  $\mu\text{m}$ .

It is clearly seen that BOE cleaning along with annealing improve the surface quality of the GGG substrate significantly. The table compares the roughness of the substrate in two different methods of cleaning.

**Table 3-2:** Roughness comparison between two different types of substrate cleaning

	<b>Roughness (rms) of Scan Area (a)</b>	<b>Roughness (rms) of Scan Area (b)</b>
Figure 3.1: GGG (Cleaned by Acetone and IPA)	1.34 nm	1.78 nm
Figure 3.2: GGG (Cleaned by Acetone, IPA, BOE, and Annealed at 1000°C)	0.526 nm	0.398 nm

We have checked the sample by SEM before cleaning and found big particles as shown in figure 3.3. We could not do the SEM after cleaning the sample because to get a clear image from SEM, thin Cr layer need to be deposited on the sample. Thus, we have checked the surface quality of clean sample only by AFM.

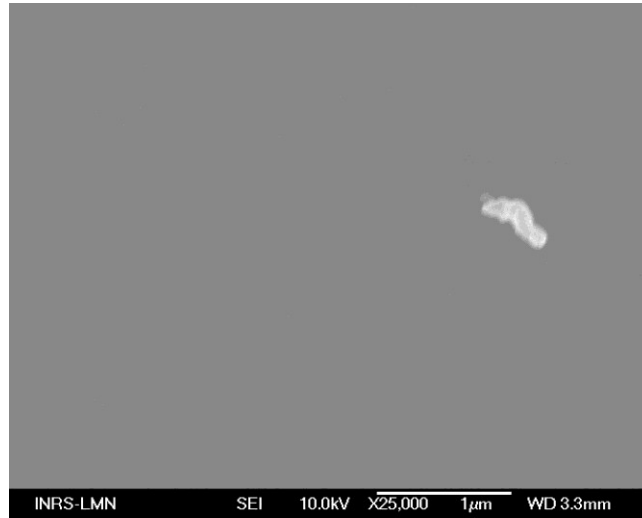


Figure 3.3: SEM image of GGG sample surface before cleaning.

### 3.3 CBN thin film deposition

In our experiment, we used PLD for CBN deposition [1, 7-8]. A two inch diameter commercially available target was bought (Kurt J. Lesker, USA) for our experiment. The target was placed inside the PLD vacuum chamber and the laser was focused on it. GGG substrates were loaded inside the chamber through a load lock, and during deposition the target and substrate distance was maintained at 6.5 cm. Both the target and substrate were rotated to have homogeneous film deposition on the substrate. Additionally, the laser were rastered using a focused lens. The optimum deposition temperature and oxygen partial pressure were 750 °C and 50 mTorr. Also, spot size was 0.06 cm<sup>2</sup>, fluence 2 J/cm<sup>2</sup>, heating and cooling rate were 20 and 10 °C/min

respectively. Under this optimum deposition condition, CBN deposition rate was 0.20 nm/s and the film thickness was measured by both SEM and Dektak profilometry. Almost similar value was found from both techniques as shown in figure 3.4 and 3.5 respectively. Highly oriented and single phase CBN films are confirmed by x-ray diffraction. XRD plots (figure 3.6 and 3.7) showed only the  $00l$  ( $l=1, 2, 3$ ) pseudocubic peaks from the CBN films and GGG substrates. For the optimization, the film was deposited under different temperature and pressure keeping the other deposition parameter such as fluence, spot size, frequency, heating and cooling rate, etc constant.

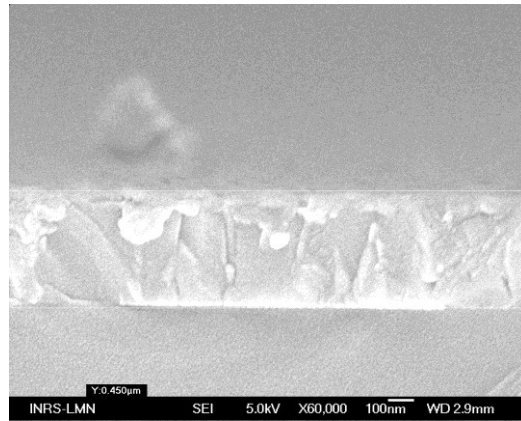


Figure 3.4: CBN thickness calibration by SEM.

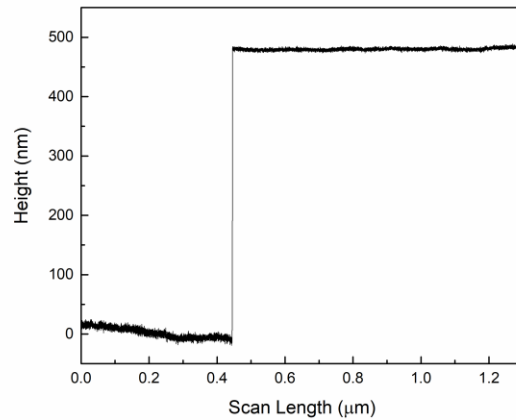


Figure 3.5: CBN thickness calibration by Dektak profilometer.

## 3.4 Experimental Results

This section describes structural and optical properties of CBN thin film deposited on GGG substrate. XRD measurements were done to check the growth direction of CBN thin films. XPS measurement provides the compositional analysis. Surface quality was checked by AFM and SEM. Optical properties of CBN thin film was measured using Ellipsometry.

### 3.4.1 Structure and Morphology

#### 3.4.1.1 XRD Analysis

The single phase structure of CBN thin film on GGG substrate is proved by X-ray diffraction measurements. As shown in Figure 3.6, the  $\theta$ - $2\theta$  scan shows very intense (001) peak where as no other secondary peaks are observable.  $\theta$ - $2\theta$  measurements were taken for all four CBN thin films deposited under four different temperatures (500, 600, 700, and 750 °C) keeping all other PLD parameters constant. CBN deposited at 750° C shows strong and intense peak with compared to others indicate that this is the optimum temperate for the crystallinity of CBN. Above 750° C secondary phase start to grow so, optimum deposition temperature is in between 700 ~ 750° C. Relatively low substrate temperature transfers insufficient energy on the adatoms to migrate on the surface, before they settle at the energetically most stable sites. As a result, the film to be crystallised with lower surface energy that may creates uneven surface morphology [9]. After that, the film was deposited under three different oxygen partial pressure (1, 50, and 100 mTorr) keeping all other PLD parameters constant. The variation of pressure modifying the mobility of the atoms ejected from the target towards the substrate [10]. In our experiment we found that film deposited at 50 mTorr is optimal since it shows the strongest and intense peak in  $\theta$ - $2\theta$  scan. XRD measurements for pressure optimization are shown in figure 3.7. At low pressure (1 mTorr)

high speed adatoms sputter from the substrate, whereas high pressure (100 mTorr) adatoms collide with oxygen molecule inside the chamber and many of them failed to reach to the substrates which significantly degrade the film quality. In conclusion, optimum deposition temperature and oxygen partial pressure are 700 ~ 750° C and 50 mTorr respectively. The other deposition parameters are spot size 0.06 cm<sup>2</sup>, fluence 2 J/cm<sup>2</sup>, frequency 20 Hz, heating rate 20° C/min, cooling rate 10° C/min, which were found as optimum for the deposition on MgO [2], and NSTO [5]. In our study, we also found similar optimum value for those parameters and detailed results are not shown here as it is already presented in Sébastien Vigne's PhD thesis (from same research group).

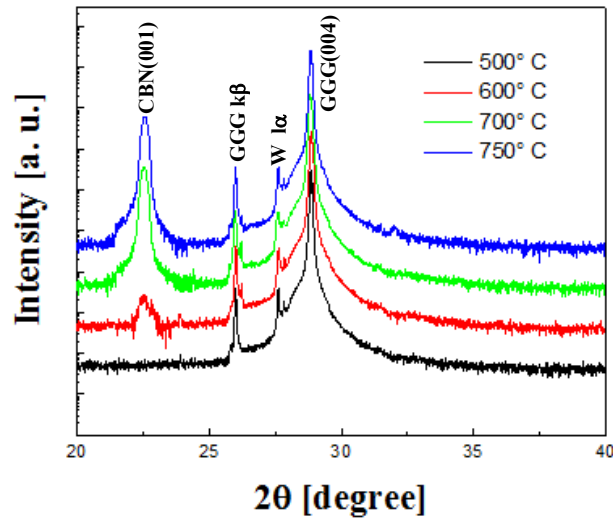


Figure 3.6: XRD  $\theta$ - $2\theta$  scans of CBN/GGG thin films grown on (001) oriented GGG substrate at the growth temperature of 500° C, 600° C, 700° C, and 750° C. Other deposition parameters such as pressure 1 mTorr and fluence 2 J/cm<sup>2</sup> were kept constant for all depositions during deposition temperature optimization. Y-axis is in logarithmic scale and offsets are created for better representation.

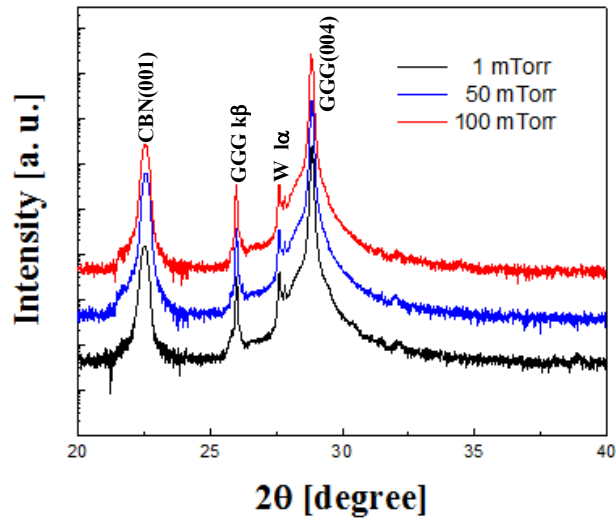


Figure 3.7: XRD  $\theta$ - $2\theta$  scans of CBN/GGG thin films grown on (001) oriented GGG substrate under the oxygen partial pressure of 1, 50 and 100 mTorr. Other deposition parameters such as temperature  $750^\circ\text{C}$  and fluence  $2\text{ J/cm}^2$  were kept constant for all depositions during pressure optimization. Y-axis is in logarithmic scale and offsets are created for better representation.

The quality of the grown films is further investigated by the Rocking Curve measurement. Figure 3.8 shows Rocking Curve measurement around the (001) peak of the CBN films as a function of deposition temperature. The FWHM of the film deposited at  $750^\circ\text{C}$  is found to be  $0.15^\circ$  which reflects a low level of mosaicity of the plans. The FWHM values in figure 3.8 clearly show that optimum deposition temperature is between  $700$  to  $750^\circ\text{C}$  which is consistent with the XRD results presented earlier.

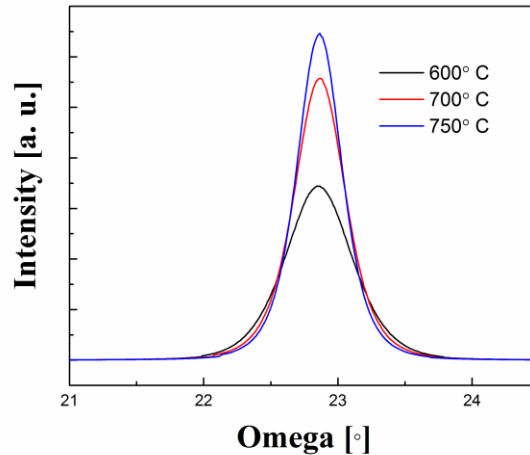


Figure 3.8: Rocking curve measurements of CBN deposited under three different temperatures. Other deposition parameters such as pressure 50 mTorr, and fluence  $2 \text{ J/cm}^2$  were kept constant for all depositions.

### 3.4.1.2 AFM Analysis

AFM analysis has been used to study the micro-structure of the thin films. AFM was used to determine the surface morphology of the films since surface roughness is an important factor for optical device performance. AFM measurements estimated the root mean square (rms) roughness of the CBN films. A  $3\mu\text{m}$  by  $3\mu\text{m}$  square area is taken into consideration for measuring the rms roughness value. Epitaxial films grown at a low oxygen pressure exhibit a low rms roughness of 1.2 nm for the films deposited at 1 mTorr, whereas thin films deposited at 50 mTorr present a rms roughness equal to 1.4 nm. Above 50 mTorr, the rms roughness significantly increases for epitaxial films to 2.9 nm at 100 mTorr as shown in table 3.3. Atomic force microscopy images show that as oxygen pressure increases, average surface roughness of the films has increases. The grain misorientaion could be the reason for high average roughness [11]. The roughness is increasing because of the grain formation which can be described by the interaction between the

ablated species and the oxygen molecules at high pressure, which significantly decreases the energy of the species impinging on the substrate, affecting both film density and surface diffusion [12]. Figure 3.9 shows the AFM images of the samples deposited under different oxygen pressure.

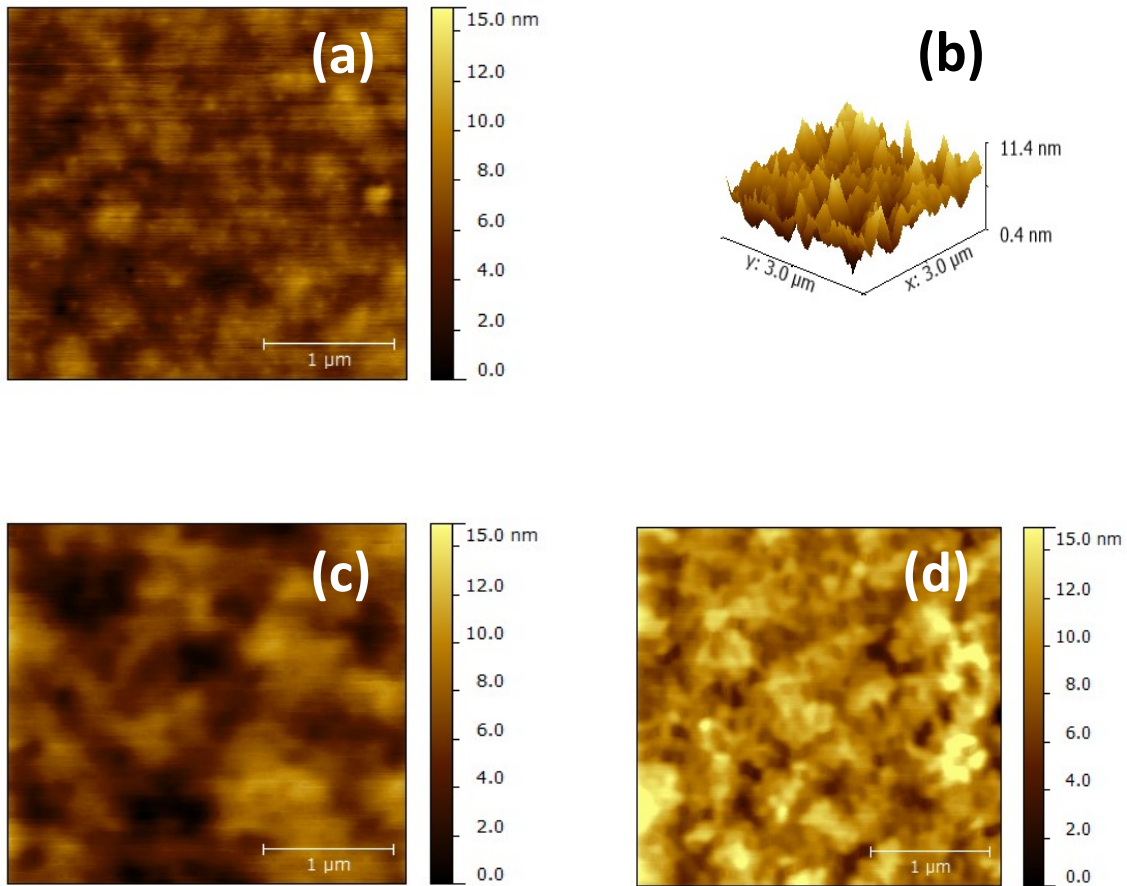


Figure 3.9: (a) (3x3 μm) AFM image of the CBN/GGG surface at 1 mTorr and (b) corresponding 3D view. (c) AFM image of sample deposited at 50 mTorr. (d) AFM image of sample deposited at 100 mTorr. Deposition temperature 750 °C and fluence 2 J/cm<sup>2</sup> were kept constant for all.

**Table 3-3:** Roughness comparison of CBN films under different growth condition

	<b>Figure 3.9 (a)</b>	<b>Figure 3.9 (c)</b>	<b>Figure 3.9 (d)</b>
Roughness (nm)	1.2	1.4	2.9

After initial free expansion from the target surface, the mean free path of the ablated particles is reduced because a high ambient gas pressure results in a low kinetic energy of the ablated species which compose the plume, following the scattering and multiple collisions occurring with oxygen atoms or molecules. In particular, more collisions and scattering occur at higher ambient pressure which reduces the mobility of the particles striking the film. These clusters do not have enough energy to migrate on the surface. Therefore, small grains, start to grow without any particular rearrangement, which results in a higher surface roughness as well as in the growth of significantly porous thin films.

### **3.4.1.3 SEM Analysis**

The surface morphology of the films confirms smooth, dense and uniform CBN thin films without any obvious droplets (Figure 3.10). Additionally, absence of micro cracks and pinholes on the CBN thin film surface confirm thermal stability. This droplet free smooth film is suitable for device applications.

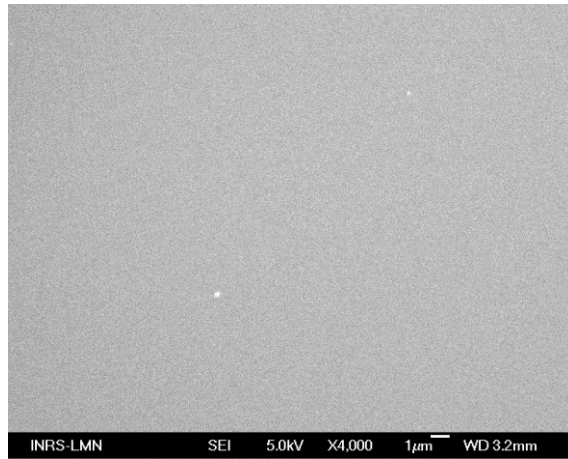


Figure 3.10: SEM top view image of the CBN films (deposited at 750 °C, 50 mTorr) on GGG substrate.

In the above figure 3.10, large area SEM image confirms CBN growth with smooth, well packed crystal grains, and crack free which is suitable for photonic applications.

#### **3.4.1.4 XPS analysis**

XPS analysis was performed on the CBN thin film deposited under optimised temperature (750°C) and pressure (50 mTorr). The determination of the exact oxygen concentration in the film remains a challenge due to the presence of oxygen in the GGG substrate [13]. The film was etched for 5 min to sputter few nm under Ar ion gun which remove the surface contamination. Figure 3.11 shows high resolution integration of the XPS scan profile from where the atomic concentration of Ca, Ba, Nb, and O is calculated. Table 3-4 shows the atomic concentration of Ca, Ba, Nb, and O with respect to etching time.

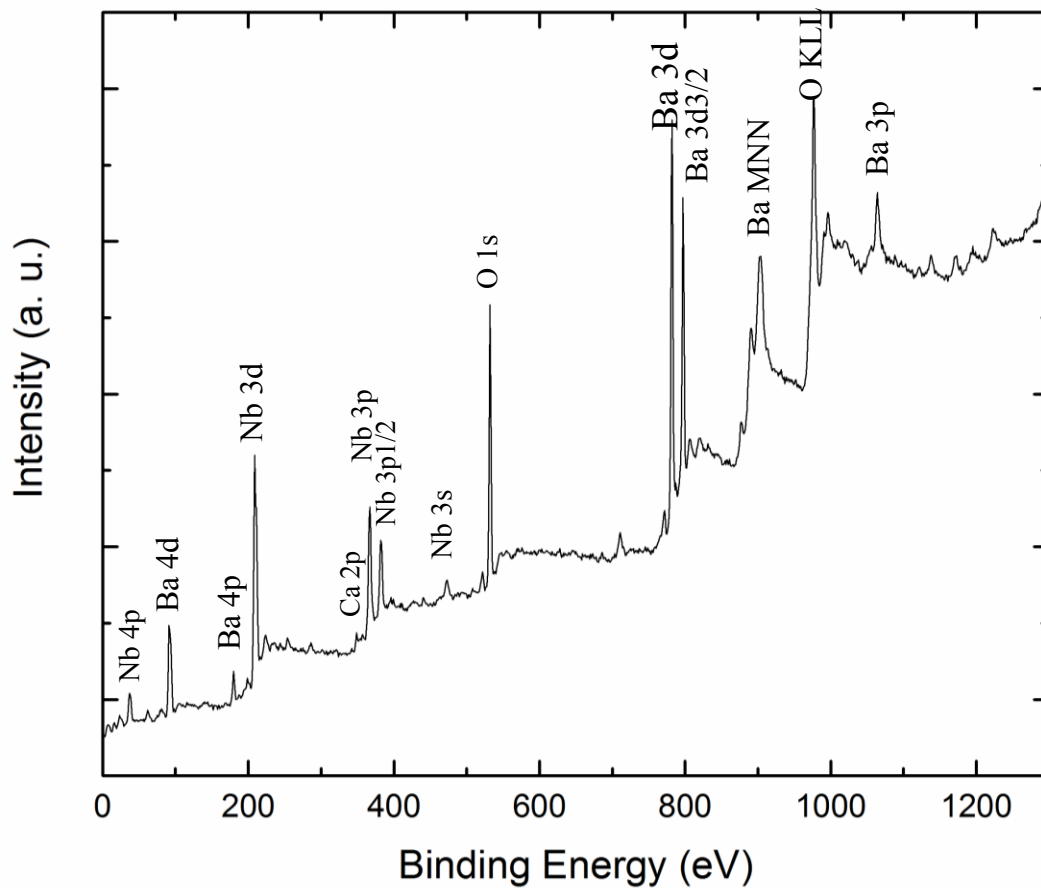


Figure 3.11: XPS spectra of the CBN films (deposited at 750°C and 50 mTorr) on GGG substrate. CBN etching time was five minutes.

**Table 3-4:** Elemental quantification (% Atomic Concentration) of CBN measured by XPS

Etching Time (min)	Ca %	Ba %	Nb %	O %
5	3.0	7.00	22.50	67.50
10	2.90	7.10	22.40	67.60
20	3.00	7.00	22.50	67.50

### 3.4.2 Optical Properties

Besides the basic structural and morphological characteristics of the deposited film, we also carried out fundamental optical characterization such as evaluation of the transparency of the material at different photon energies. Figure 3.12 shows a high transmission (>85%) for wavelengths above 400 nm and for thin films deposited at a pressure of 50 mTorr. On the other hand, films deposited at 100 mTorr show a weaker transmission (<50%) at 400 nm. The weak transmission observed for 100 mTorr films may be due to the high surface roughness and to the possible presence of some porosity inside the films, which can dramatically deteriorate the optical quality of the samples especially at lower wavelengths as reported in Reference 2. A much weaker transmission at 1 mTorr suggest the possibility of presence of some void networks at this non-optimum pressure as well as the optimum deposition pressure is somewhere close to 50 mTorr.

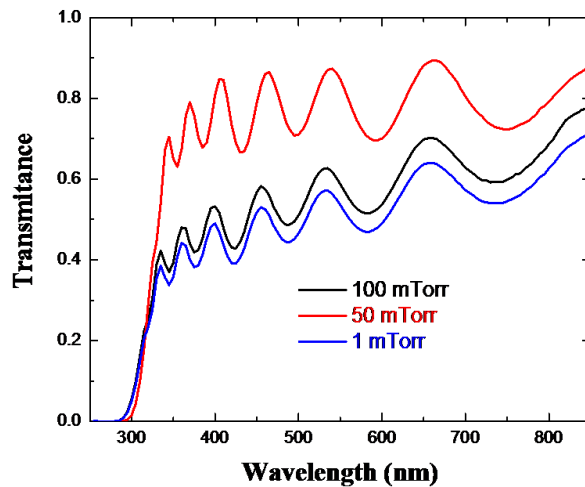


Figure 3.12: Optical transmittance of CBN thin film on GGG substrate with the variation of deposition pressure (1, 50, and 100 mTorr). Keeping all other deposition pressure same (temperature 750° C, fluence 2 J/cm<sup>2</sup>, frequency 20 Hz etc).

### **3.5 Conclusion**

In conclusion, CBN thin film was deposited and optimised on GGG substrate under various deposition conditions such as variation of pressure and temperature. The optimum deposition temperature and pressure is found as 700° C ~ 750° C and 50 mTorr respectively. X-ray diffraction verifies the crystal quality of the film, whereas surface quality is measured by both AFM and SEM. Chemical composition was determined by XPS analysis.

### 3.6 References

1. R. Helsten, et al., "Pockels response in calcium barium niobate thin films", Applied Physics Letters, 91, 261101, (2007).
2. Paul F. Ndione, et al., "Structural and optical properties of epitaxial  $\text{Ca}_x\text{Ba}_{1-x}\text{Nb}_2\text{O}_6$  thin films grown on MgO by pulsed laser deposition", Journal of Applied Physics, 103, 033510, (2008).
3. S. Vigne, et al., "Investigation of nickel as hard mask for patterning multicomponent oxide materials in chlorine plasmas", Journal of Applied Physics, 114, 10, (2013).
4. F. Fesharaki, et al., "Theoretical Analysis and Experimental Evaluation of  $\text{SiO}_2$ -CBN-MgO Rib Waveguide Structure", IEEE Photonics Technology Letters, 26, 18, (2014).
5. S. Vigne, et al., "Optical properties of epitaxial  $\text{Ca}_x\text{Ba}_{1-x}\text{Nb}_2\text{O}_6$  thin film based rib-waveguide structure on (001) MgO for electro-optic applications," Optics Express, 24, 25, (2016).
6. R. Helsten, et al., "Pockels response in calcium barium niobate thin films", Applied Physics Letters, 91, 261101, (2007).
7. Hideki Yokoi, et al., "Optical nonreciprocal devices with a silicon guiding layer fabricated by wafer bonding," Applied Optics, 42, 33, (2003).
8. C.L. Jia et al., "Tailoring the orientations of complex niobate films on perovskite substrates", Acta Materialia, 54, 9, (2006).
9. S.B. Mi et al., "Growth of  $\text{Ca}_x\text{Ba}_{1-x}\text{Nb}_2\text{O}_6$  thin films on MgO (100) by pulsed laser deposition", Journal of Crystal Growth, 291, 243–248, (2006).

10. J.-II Hong, "Room-temperature, texture-controlled growth of ZnO thin films and their application for growing aligned ZnO nanowire arrays", *Nanotechnology*, 20, 085609, (2009).
11. P.R. Willmott, "Deposition of complex multielemental thin films", *Progress in Surface Science*, 76, 163–217, (2004).
12. Aghabagheri, et al., "Effect of Oxygen Pressure on the Surface Roughness and Intergranular Behavior of YBCO Thin Films", *J Supercond Nov Magn*, 29, 1483, (2016).
13. Teruaki Suzuki, et al., "Reverse-rotational domains in in-plane switching-mode liquid crystal displays", *Journal of Applied Physics*, 89, 1, (2001)
14. M. Cuniot-Ponsard, et al., "Radio frequency magnetron sputtering deposition of hetero-epitaxial strontium barium niobate thin films ( $\text{Sr}_x\text{Ba}_{1-x}\text{Nb}_2\text{O}_6$ )", *Journal of Applied Physics*, 93, 1718, (2003).

# Chapter 04

## Grating Coupler Fabrication

### 4.1 Introduction

The coupling of light to an optical fiber is challenging because of the small size of nanophotonic waveguides. The large inherent size mismatch between the light mode in fiber and a waveguide means that an enormous amount of power will necessarily be lost when trying to move the signal directly from fiber to the waveguide end. Figure 4.1 shows the measured total waveguide loss of a CBN thin film based rib waveguide as a function of waveguide length, which we reported recently in reference [1]. During this measurement light was coupled to the waveguide structure using end-fire coupling technique. An extrapolation of total waveguide loss curve to zero waveguide length provides insertion/facet loss. It is measured at 12.3 dB, which is very high, but consistent with the end-fire coupling technique. This huge facet loss is one of the key obstacles to demonstrate device operation. Additionally, the aperture differences between the two systems hamper efficiency when coupling light out of the nanophotonic device.

To overcome this problem, many different solutions have been proposed and demonstrated in recent years. One of them is to use different mode-size converters which may couple light from large fibre mode to a small waveguide mode. However, smallest mode size from a commercial mode coupler is around 2-3  $\mu\text{m}$ , which is still far from ideal and not perfect for nm thickness thin film based waveguides. An increase in the thin film thickness may be a solution. But in our case, an increase in CBN film thickness will degrade the film quality and hence reduce the functional

properties of the material, such as the electro-optic coefficient. In this work, we investigated the fabrication of a CBN thin film based optical grating coupler coupled with CBN thin film waveguide to improve the light coupling efficiency. Grating coupler, a region on top of or below a waveguide where there is a grating, is a kind of structure in which guided-mode resonance takes place. Once designed accurately, resonance happens for specific combinations of incident angles and light frequency and allows the grating to couple light into a guided mode of the waveguide [2]. The following sections describe the fabrication and characterizations of the CBN thin film based optical grating coupler.

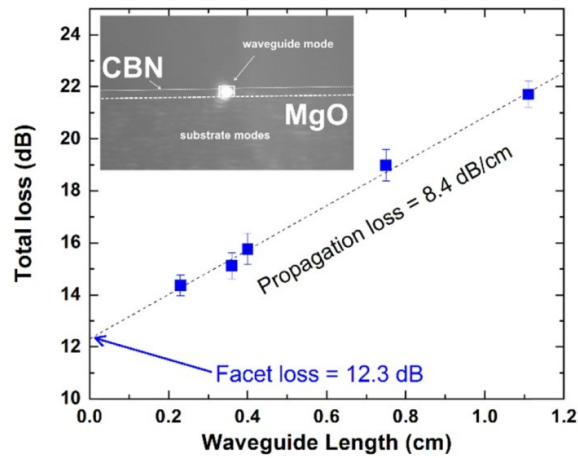


Figure 4.1: Total loss as a function of waveguide length to estimate the facet loss and propagation loss.

(inset) Typical mode profile at the output of the waveguide [1].

## 4.2 Grating coupler fabrication procedures

For grating coupler fabrication we took a 1  $\mu\text{m}$  thick CBN thin film deposited on a GGG substrate. CBN was deposited using PLD under the deposition conditions of temperature 750° C, pressure 50 mTorr, spot size 0.06  $\text{cm}^2$ , fluence 2  $\text{J}/\text{cm}^2$ , frequency 20 Hz, etc. The process of CBN/GGG grating coupler fabrication is depicted on figure 4.2. The fabrication process mainly

consists of two times CBN etching. Initially, CBN is etched for grating and then, CBN is etched for wave guides. For both etching same procedures are followed. CBN etching mainly has 9 individual steps.

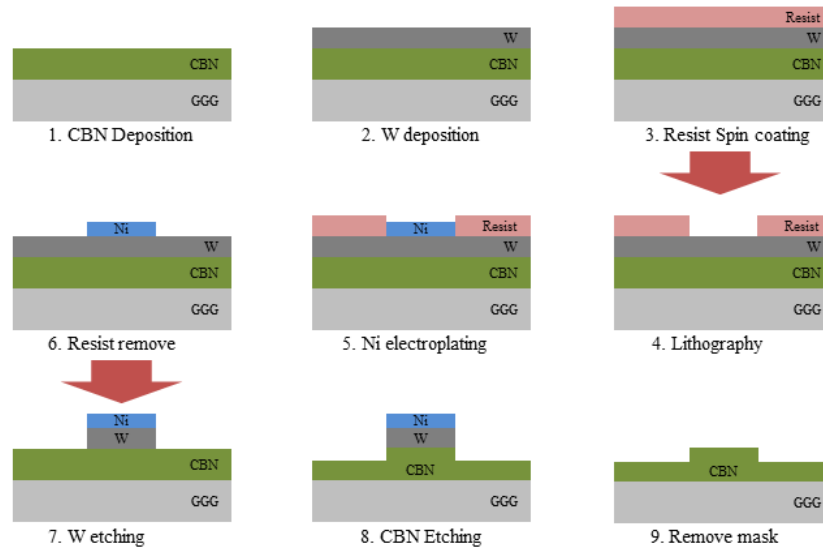


Figure 4.2: Schematic representation of CBN etching for grating coupler fabrication on GGG.

At first, CBN thin film on GGG substrate is cleaned in acetone and then IPA bath followed by drying with a nitrogen spray gun. Secondly, 100 nm tungsten (W) is deposited on CBN using sputtering systems CMS-18 (manufacturer: Kurt J. Lesker). We selected W rather than other metals such as Cu or Cr because it is possible to chemically etch W in a basic solution of  $\text{NH}_4\text{OH} + \text{H}_2\text{O}_2$  diluted in water that does not attack the substrate of GGG. Moreover, the plasma etching of the W is known and optimized, which also enabled us to perform step 7 of figure 4.2 without any problem. The main role of this W layer is to deposit a Ni hard mask on it as Ni deposition using electroplating requires a conductive layer. Thirdly, e-beam resist is spin coated on top of W and patterned with Electron Beam Lithography (EBL) (Vistec VB6 UHR-EWF). Then, Ni is deposited as a hard mask by electroplating method. We have noticed that nickel

deposited by electroplating from nickel sulphamate solution is less stressed in comparison to evaporated films, which is greatly favorable for holding the Ni mask during etching. Figure 4.3 shows clear SEM images of electroplated Ni hard mask on top of W.

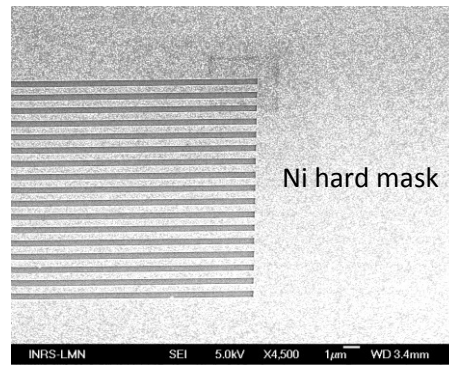


Figure 4.3: SEM image of electroplated Ni mask

After that resist is removed by selective remover which opens the area of W etching. Inductively Coupled Plasma – Reactive Ion Etching (ICP-RIE) (Oxford PlasmaLab System100) were used for the W etching. W is etched from everywhere of the sample which opens up CBN underneath of it. The optical end-point detection system stops the etching process when the underneath CBN layer is reached. Then CBN is also etched using Inductively Coupled Plasma – Reactive Ion Etching (ICP-RIE) (Oxford PlasmaLab System100). CBN etching depth is controlled using the optical end-point detection system. Approximate etching depth for the grating pattern is 250 nm and etching rate of 30 nm/min. Finally, the sample is kept in  $\text{NH}_4\text{OH} + \text{H}_2\text{O}_2$  diluted in water for few hours to remove the W which completes the CBN etching. With the above mentioned process we have completed CBN patterning for both the grating and alignment mark in the four corners of the sample at the same time. Next, similar steps are repeated for waveguide patterning

except that we have used e-beam resist ZEP520A for the wave guide patterning. Corner alignment marks were used to align the wave guides with the grating pattern.

### 4.3 Grating Coupler Characterizations

A grating coupler with a period of 400 nm and etch depth of 250 nm was fabricated. The period and each depth value were calculated based on the simulation technique reported in reference [2]. For characterization purposes grating couplers were coupled to CBN rib waveguide structure as shown in the block diagram in Figure 4.4.

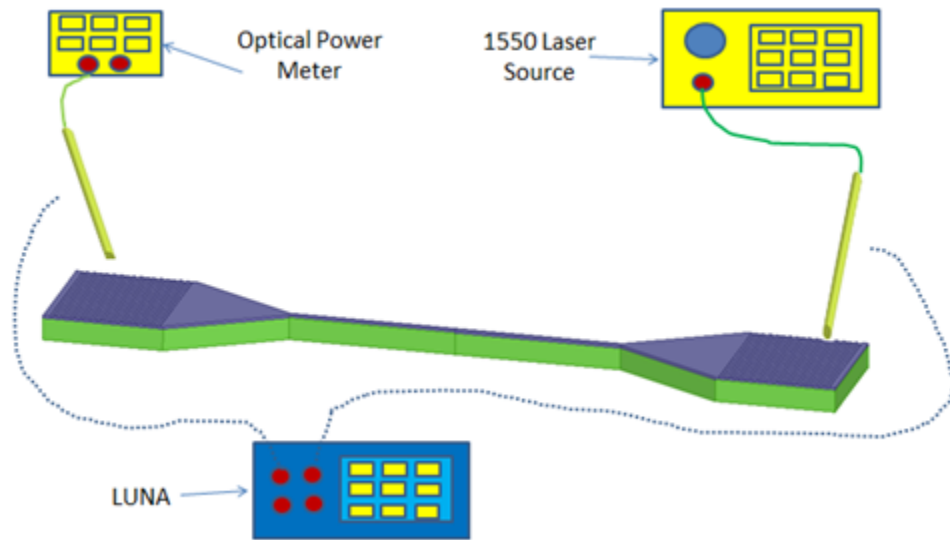


Figure 4.4: Block diagram of optical grating coupler characterization setup.

A chip containing various sets of optical grating coupler coupled to CBN rib waveguide structure with different waveguide lengths was placed on an adjustable mount on XYZ stage. First light was coupled to the optical grating coupler from a 1550 nm laser source. This coupled light propagates through the rib waveguide structure and decoupled by the other ends grating coupler

and measured by an optical power meter. A top view camera and a side view camera attached to ViewSonic computer software were used for the alignment of grating coupler device chip, input and output fiber. The coupling angle was varied from  $7^\circ$  to  $15^\circ$  and output light power was measured from where we determined an optimum coupling angle around  $10^\circ$ . At the optimum coupling angle maximum amount of light is coupled to the grating coupler and propagates through the waveguide structure. For every device, the height of the input and output fiber was also adjusted to reduce noise. Once the device position, input/output fiber height and coupling angle was optimized, input and output fiber end was connected to Luna vector analyzer system to measure the total power loss as a function of wavelength as shown in Figure 4.5 (a).

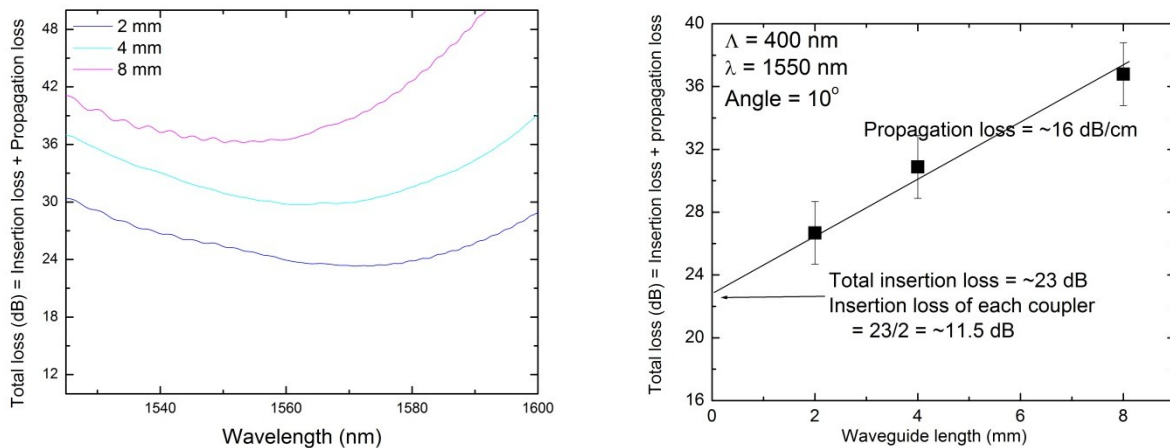


Figure 4.5: (a) Total loss as a function of wavelength for various waveguide lengths measured by LUNA vector analyzer system. (b) Total loss as a function of waveguide length.

Figure 4.5(a) shows measured total loss (grating coupler insertion loss + waveguide propagation loss) as a function of wavelength for waveguide length 2, 4 and 8 mm. A system loss of 3 dB is already subtracted from the original measured data. Figure 4.5(b) shows total loss as a function of waveguide length. An extrapolation of total loss vs waveguide data to zero waveguide length gives total insertion loss of  $\sim 11.5$  dB per coupler. This value is significantly higher than that of

conventional SOI based grating couplers [2]. However, the ability to couple light in CBN rib waveguide structure via a CBN grating coupler shows a great promise for the integration of this new material for high performance EO device application. From the slope of total loss vs waveguide data we found a propagation loss of 16 dB/cm, which is much higher than that of CBN/MgO and CBN/Si based waveguide structures [2]. It may be due to the high sidewall roughness during the etching.

#### **4.4 Conclusion**

We have experimentally demonstrated functional grating coupler and we have coupled light successfully. The measured insertion loss and propagation loss of CBN rib waveguide structure is found to be ~11.5 dB per coupler and ~16 dB/cm. The ability to couple light in CBN rib waveguide structure via CBN grating coupler shows a great promise for the integration of this new material for high performance EO device application.

## 4.5 References

1. S. Vigne, et al., “Structural and optical properties of  $\text{Ca}_x\text{Ba}_{1-x}\text{Nb}_2\text{O}_6$  thin films deposited by radio frequency magnetron sputtering”, *Optical Materials Express*, 5, 11, (2015).
2. Faezeh Fesharaki, et al., “Accurate theoretical and experimental characterization of optical grating coupler”, *Optics Express*, 24, 18, (2016).

## Chapter 5

### Conclusion and Future Work

We investigated the synthesis of CBN thin films on lattice matched (001) GGG substrate to grow highly oriented CBN. Growth of epitaxial CBN on GGG was performed by Pulsed Laser Deposition (PLD) at 750° C under an oxygen pressure of 50 mTorr, spot size was 0.06 cm<sup>2</sup>, fluence 2 J/cm<sup>2</sup>, heating and cooling rate were 20 and 10° C/min respectively. The CBN thin film is highly textured in the (001) orientation, as well as a transparency of the film >85% is observed, which represents a significant improvement of the crystalline quality of CBN deposited on GGG. Finally, we have successfully fabricated and demonstrated light coupling through a CBN thin film based optical grating coupler to CBN thin film based waveguides on GGG substrate. The measured insertion loss and propagation loss of CBN rib waveguide structure is found to be ~11.5 dB per coupler and ~16 dB/cm. The ability to couple light in CBN rib waveguide structure via CBN grating coupler is a further step towards the integration of CBN thin film for high performance EO device application.

Although this work reports a significant progress in the synthesis of CBN/GGG thin film materials as well as fabrication of CBN thin film based optical grating couplers, waveguides etc. but active photonic devices yet to be demonstrated. Further work is required for the optimization of CBN film on conductive GGG substrate to evaluate EO performance towards the further optimization of materials functional properties. EO modulators need to be demonstrated using the CBN thin film deposited on GGG. The high insertion loss and propagation loss observed in

CBN/GGG thin film based grating couplers and waveguides, respectively need to be improved further by improving the fabrication method.

## Résumé

# Synthèse par ablation laser de couches minces de $\text{Ca}_x\text{Ba}_{1-x}\text{Nb}_2\text{O}_5$ sur un substrat de GGG (réseau cristallin compatible avec le CBN)

### 1. Introduction

L'essor des besoins en échange d'information requiert le développement de systèmes de transfert de données performants pour les télécommunications. Les matériaux en couches minces ayant des coefficients électro-optiques (EO) élevés sont attractifs pour la fabrication de composants photoniques de haute performance, tels que les modulateurs EO pour les applications en télécommunications. Le matériau  $\text{Sr}_x\text{Ba}_{1-x}\text{Nb}_2\text{O}_6$  (SBN), de la famille des ferroélectriques Tetragonal Tungsten Bronze (TTB) possède le coefficient electro-optique le plus élevé, aussi bien sous forme massive qu'en couche mince. Comparativement au niobate de lithium commercial ( $\text{LiNbO}_3$ , LN), le SBN a un coefficient EO quarante fois plus élevé. Néanmoins, du fait de sa faible température de Curie (en-dessous de  $80^\circ\text{C}$ ), le SBN n'est pas approprié pour être utilisé comme couche active dans les modulateurs EO fonctionnant dans des gammes de fréquences de quelques centaines de GHz. Par contre, le  $\text{Ca}_x\text{Ba}_{1-x}\text{Nb}_2\text{O}_6$  (CBN), qui appartient également à la famille des TTB, a un coefficient EO (130 pm/V) et une température de Curie

(au-dessus de 200°C) élevée. Ce matériau constitue donc un candidat potentiel pour la prochaine génération de dispositifs pour les applications électro-optiques.

Des films minces épitaxiés de CBN ont été synthétisés sur différents types de substrats, notamment MgO, Nb:SrTiO<sub>3</sub>, ainsi que Si. Cependant les films épitaxiés de CBN doivent être déposés sur des substrats ayant un réseau cristallin favorable et qui soient compatibles avec les procédés de fabrication de dispositifs (l'indice de réfraction du substrat doit être plus faible que celui du CBN). Ces conditions doivent être réunies afin que les films épitaxiés de CBN puissent être intégrés dans des dispositifs de haute performance. L'objectif de ce travail est d'étudier la synthèse de couches minces de CBN sur un nouveau type de substrat à savoir le Gadolinium Gallium Garnet (Gd<sub>3</sub>Ga<sub>5</sub>O<sub>12</sub>, GGG) dont le réseau cristallin est compatible avec celui du CBN.

## **2. Les matériaux ferroélectriques**

Il existe une sous-classe de la classe des matériaux diélectriques polaires pour laquelle la polarisation spontanée peut être réorientée sous l'action d'un champ électrique d'amplitude suffisante. Dans le cas de ces matériaux, la polarisation ne retourne pas spontanément à son état initial après annulation du champ électrique appliqué. Ces matériaux sont dits ferroélectriques. Les relations entre les groupes de diélectriques ferroélectriques, polaires, acentriques et centrosymétriques sont indiquées dans le diagramme de Venn ci-dessous sur la figure 1.

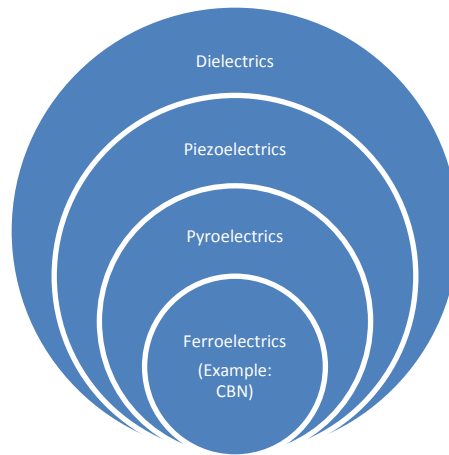


Figure 1: Diagramme de Venn montrant les ferroélectriques parmi les différentes classes de matériaux diélectriques.

Les matériaux ferroélectriques sont caractérisés par le fait que la polarisation peut être renversée par l'application d'un champ électrique. La mesure expérimentale de la polarisation en fonction du champ électrique décrit un cycle d'hystérésis qui permet d'identifier certains paramètres caractéristiques tels que la polarisation à saturation, la polarisation rémanente et le champ coercitif.

### 3. Matériaux ferroélectriques et applications

Les matériaux ferroélectriques sont largement utilisés pour de nombreuses applications telles que les condensateurs, les piézoélectriques pour l'imagerie ultrasonore, les thermistances, les commutateurs RF, les oscillateurs, filtres, les varacteurs pour les circuits RF microondes, les diélectriques, les matériaux à haute constante diélectrique, les mémoires FeRAM, les jonctions Tunnel ferroélectriques, les matériaux multiferroïques, les transducteurs piézoélectriques, les détecteurs pyroélectriques, les déflecteurs de lumière, les matériaux électro-optiques pour les

applications en stockage de données. La figure 2 montre les applications en électronique intégrant les couches minces ferroélectriques.

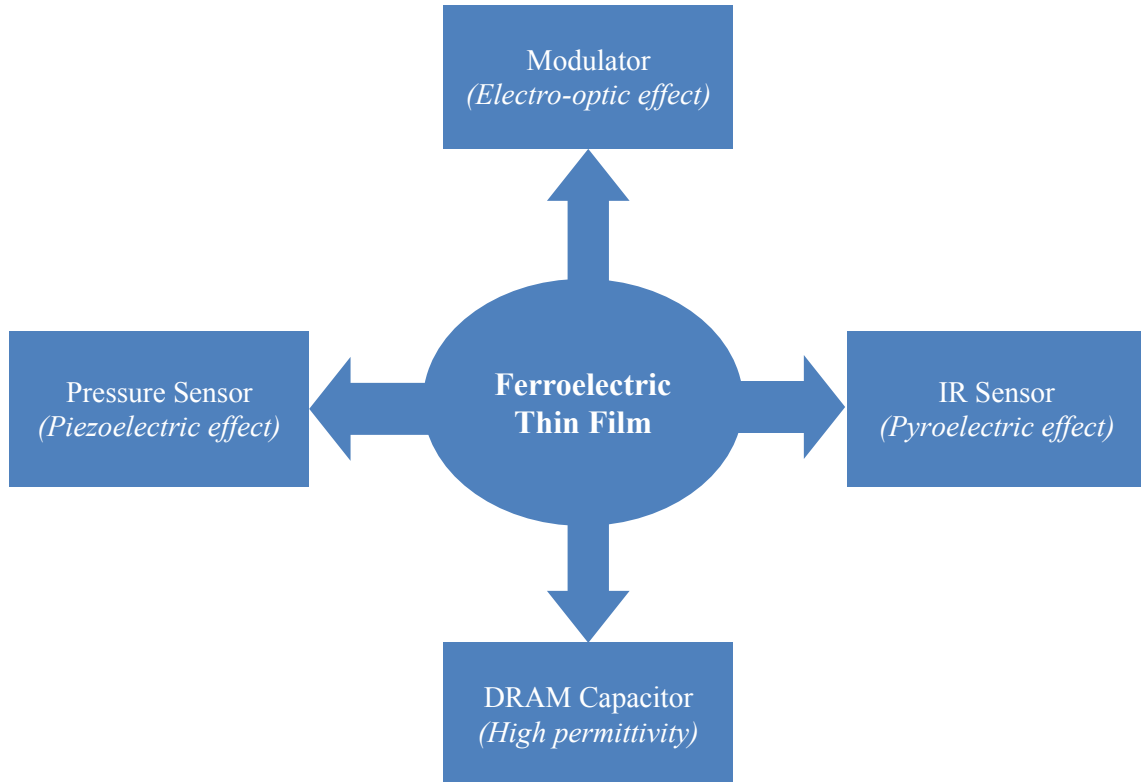


Figure 2: Applications incluant des composants à base de couches minces ferroélectriques.

#### 4. Synthèse des couches minces de CBN

Dans le cadre de nos travaux, nous avons utilisé l'ablation laser (ou PLD) pour le dépôt du CBN [1-3], à partir d'une cible commerciale ayant un diamètre de 2 pouces. La cible est positionnée dans l'enceinte sous vide de façon que le faisceau laser soit focalisé sur sa surface. Les substrats GGG sont positionnés à l'intérieur de l'enceinte sous vide à travers un sas de transfert. Durant le

dépôt, la distance entre la cible et le substrat est de 6.5 cm. Afin d'obtenir une érosion homogène de la cible et d'assurer une plus grande uniformité de la couche mince déposée sur le substrat, la cible et le substrat sont tous les deux en rotation durant le dépôt. De plus, à la rotation de la cible, est couplé un balayage laser à l'aide d'un miroir oscillant. Nous avons trouvé que la température et la pression partielle d'oxygène optimales de dépôt sont respectivement de 750°C et de 50 mTorr,. Par ailleurs, la surface de la tache focale est de 0.06 cm<sup>2</sup> et la fluence de 2 J/cm<sup>2</sup>. Les vitesses des séquences de chauffage et de refroidissement sont respectivement de 20 et de 10° C/min.

Dans ces conditions optimales, la vitesse de dépôt du CBN est de 0.20 nm/s. L'épaisseur du film est mesurée en utilisant d'une part un microscope électronique à balayage (MEB) et d'autre part un profilomètre Dektak. Les analyses par diffraction des rayons X confirment une forte orientation de films monophasés de CBN. En effet, les diffractogrammes montrent que seule la signature des phases pseudo-cubiques  $00l$  ( $l=1, 2, 3$ ) du CBN et du substrat GGG est présente. Le travail d'optimisation global de l'élaboration des films de CBN s'est fait sous forme d'optimisation paramètre par paramètre : en faisant varier un paramètre tout en maintenant les autres constants à chaque fois. Les paramètres mis en jeu sont : la fluence, la surface de la tache focale, le taux de répétition du laser, la pression, la valeur et les vitesses de montée et descente de la température du substrat.

#### **4.1 Analyses par diffraction des rayons X**

La structure monophasée du film de CBN sur substrat GGG est mise en exergue à travers les analyses par diffraction des rayons X. Sur la figure 3, nous avons reporté les diffractogrammes

en  $\theta$ - $2\theta$  obtenus à quatre températures de substrat différentes (500° C, 600° C, 700° C et 750° C) et où tous les autres paramètres sont maintenus constants. Ces diffractogrammes montrent que seule la signature de l'orientation (001) du CBN est présente avec une absence de toute autre orientation secondaire. La comparaison des résultats montre, à travers la forme et l'amplitude des pics d'orientation que la température optimale de dépôt est de 750° C. En effet, une température relativement faible du substrat résulte en un transfert d'énergie insuffisant aux adatoms pour que ceux-ci migrent sur la surface avant de se fixer sur les sites les plus énergétiquement stables. Ceci empêche la cristallisation du film avec des énergies de surface plus faibles qui peuvent par ailleurs causer une morphologie de surface non-régulière [4]. Au-delà de 750° C, il commence à apparaître une phase secondaire, ce qui situe la température optimale entre 700 ~ 750° C.

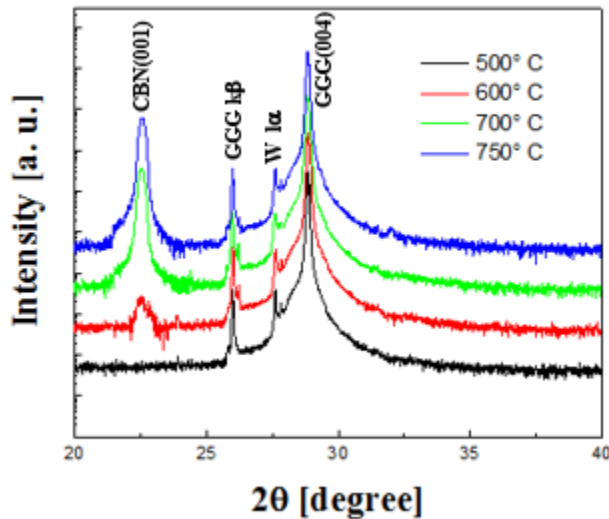


Figure 3: Diffractogrammes  $\theta$ - $2\theta$  des films CBN déposés sur substrat GGG (001) à différentes températures (500° C, 600° C, 700° C et 750° C). Les autres paramètres de dépôt sont fixes : pression=1 mTorr et fluence=2 J/cm<sup>2</sup>.

Par la suite, les films de CBN ont été déposés à trois pressions partielles d'oxygène (1, 50, and 100 mTorr), les autres paramètres gardés fixes. La variation de la pression se traduit par la modification de l'énergie des adatoms incidents sur le substrat. En effet, à mesure que la pression est augmentée, les adatoms sont freinés par les collisions avec les atomes d'oxygène [5]. Nos expériences montrent que le film déposé à 50 mTorr est optimal car caractérisé par le pic d'orientation (issu du balayage en  $\theta$ - $2\theta$ ) le plus intense

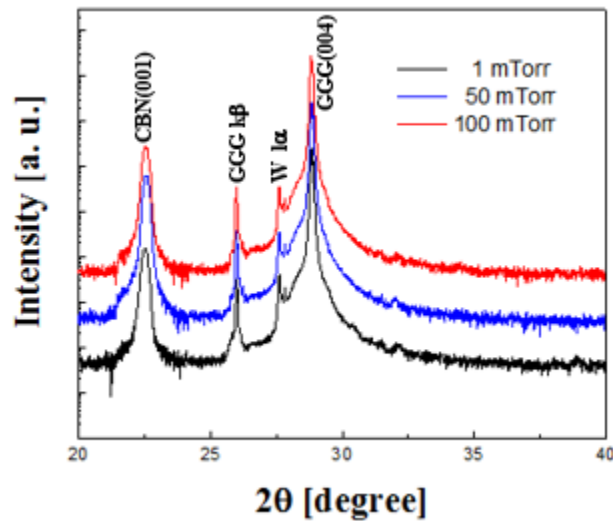


Figure 4: Diffractogrammes  $\theta$ - $2\theta$  des films CBN déposés sur substrat GGG (001) à différentes pressions partielles d'oxygène (1, 50 and 100 mTorr). Les autres paramètres de dépôt sont fixes : température= $750^{\circ}$  C et fluence= $2 \text{ J/cm}^2$ .

À faible pression (1 mTorr), il y a une pulvérisation à forte vitesse des adatoms vers le substrat tandis qu'à haute pression (100 mTorr), les adatoms ont trop faible énergie pour avoir une mobilité suffisante assurant ainsi une bonne cristallinité. En résumé, la température et la pression partielle optimales de dépôt sont respectivement de  $700 \sim 750^{\circ}$  C et de 50 mTorr. Les autres

paramètres de dépôts sont les suivants : surface de la tache focale de  $0.06 \text{ cm}^2$ , fluence de  $2 \text{ J/cm}^2$ , taux de répétition du laser de  $20 \text{ Hz}$ , vitesse de chauffage de  $20^\circ \text{ C/min}$ , vitesse de refroidissement de  $10^\circ \text{ C/min}$ . Ces paramètres ont été déterminés à travers des expériences précédentes de croissance sur des substrats MgO [5] et NSTO [6]. Nos expériences confirment le caractère optimal de ces paramètres.

La qualité cristalline des films de CBN a été analysée davantage par la mesure en Rocking Curve. La figure 5 montre la mesure autour du pic (001) des films de CBN en fonction de la température de dépôt. La largeur à mi-hauteur (FWHM) du pic du film déposé à  $750^\circ\text{C}$  a été déterminée comme étant de  $0.15^\circ$ , ce qui reflète un faible niveau de mosaïcité des plans. La comparaison des largeurs à mi-hauteur sur la figure 5 montre clairement que la température optimale de dépôt du CBN se situe entre  $700$  et  $750^\circ\text{C}$ , ce qui est conforme aux résultats d'analyses en  $\theta$ - $2\theta$  présentés plus haut.

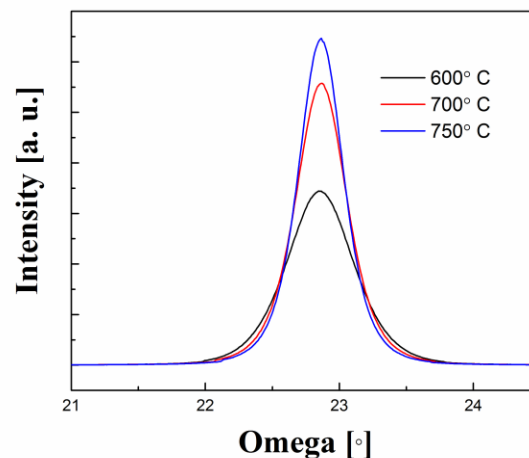


Figure 5: Analyse par Rocking curve des films CBN déposés à différentes températures. Les autres paramètres de dépôt sont fixes : pression= $50 \text{ mTorr}$  et fluence= $2 \text{ J/cm}^2$ .

## 4.2 Analyses MEB

La morphologie de surface observée par analyse MEB révèle des films de CBN denses et uniformes, avec absence de gouttelettes (Figure 6). De plus, les films de CBN ne comportent pas de microfissures ou petits trous en surface, ce qui démontre leur stabilité thermique. Ces films ont les qualités de surface requises pour leur intégration dans des dispositifs photoniques fonctionnels.

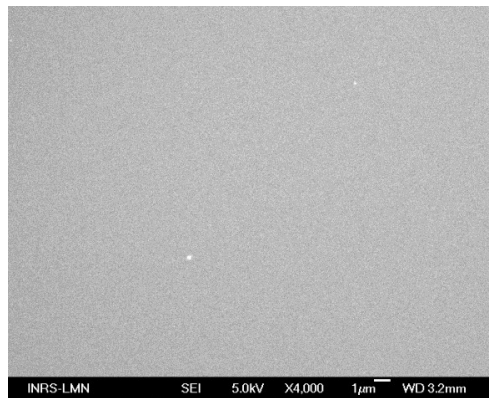


Figure 6: Image MEB de surface d'un film CBN (déposé à 750°C/50 mTorr) sur substrat GGG.

## 4.3 Propriétés optiques

En plus des caractérisations structurales des films déposés, des caractérisations optiques fondamentales telles que l'évaluation de la transparence du matériau à différentes énergies photoniques ont été réalisées. La figure 7 montre pour les films déposés à une pression de 50 mTorr une forte transmission (>85%) pour des longueurs d'ondes supérieures à 400 nm. En revanche, les films déposés à 100 mTorr ont une transmission plus faible (<50%) à 400 nm. La faible transmission observée pour ces films est potentiellement due à la forte rugosité de surface et à la probable présence de quelques porosités à travers la couche, ce qui peut détériorer de façon dramatique la qualité optique des films, en particulier à des longueurs d'ondes faibles, tel

que reporté en référence 5. Ceci est conforme aux résultats obtenus par diffraction X qui montrait une moins bonne cristallinité à cette haute pression. Une transmission encore plus faible pour les films déposés à 1 mTorr suggère la possibilité de la présence de défauts structuraux dans le réseau cristallin, à cette faible pression considérée comme étant non-optimale.

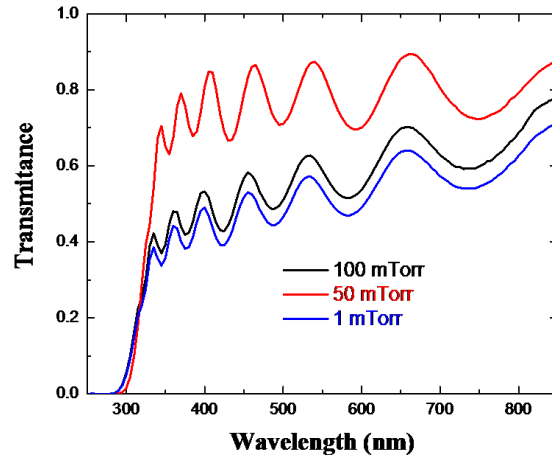


Figure 7: Transmittance des films de CBN déposés sur substrat GGG à différentes pressions (1, 50, and 100 mTorr). Les autres paramètres de dépôt sont : température=750° C, fluence=2 J/cm<sup>2</sup>, taux de répétition du laser =20 Hz).

## 5. Procédé de fabrication d'un coupleur de réseau

Pour la fabrication du coupleur de réseau, un film épais de CBN (1  $\mu\text{m}$ ) a été déposé sur un substrat GGG. Le dépôt par ablation laser a été fait sous les conditions de température de 750 °C, une pression de 50 mTorr, une surface de la tache focale de 0.06 cm<sup>2</sup>, une fluence 2 J/cm<sup>2</sup> et un taux de répétition du laser de 20 Hz. Le procédé de fabrication du coupleur de réseau CBN/GGG est décrit sur la figure 8. Le procédé de fabrication consiste essentiellement en deux étapes de

gravure du CBN. Initialement, le CBN est gravé pour le réseau, ensuite le CBN est gravé pour les guides d'ondes. Pour les deux gravures, le même procédé est utilisé. La gravure du CBN se fait suivant 9 principales étapes.

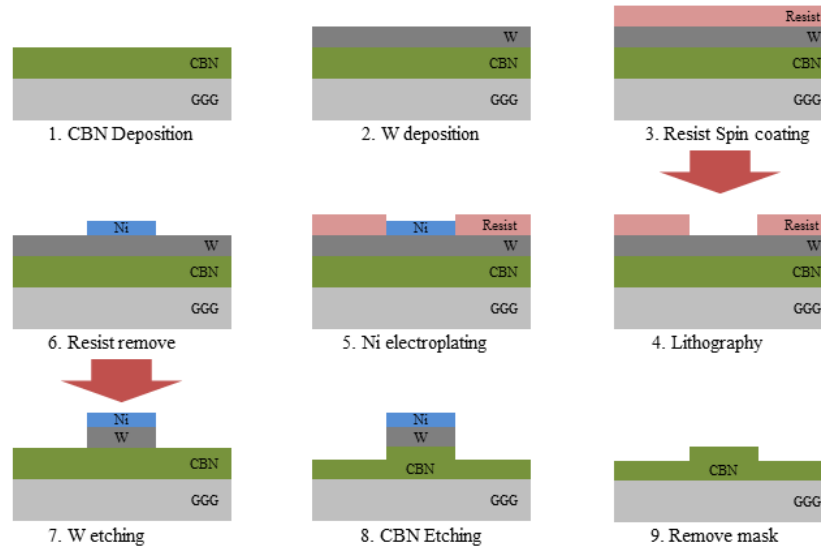


Figure 8: Représentation schématique de la fabrication d'un coupleur de réseau à base de CBN sur un substrat de GGG.

D'abord, le film de CBN/GGG est nettoyé dans un bain acétone suivi d'un bain isopropanol avant d'être séché par l'azote. La seconde étape consiste à déposer une couche W de 100 nm d'épaisseur sur la couche de CBN par pulvérisation cathodique (CMS-18 de Kurt J. Lesker). Le W a été préféré à d'autres métaux tels que Cu ou Cr parce qu'il est possible de graver chimiquement le W dans une solution basique de  $\text{NH}_4\text{OH} + \text{H}_2\text{O}_2$  diluée dans l'eau et qui n'attaque pas le substrat GGG. De plus, la gravure plasma du W est maîtrisée et optimisée, ce qui a permis d'effectuer l'étape 7 de la figure 8 sans difficulté. Le rôle principal de la couche de W est de permettre le dépôt par électroplaquage du masque dur de Ni. Ensuite, la résine électronique MA-N est déposée par centrifugation sur la surface du W et exposée par EBL

(Electron Beam Lithography) Vistec VB6 UHR-EWF. Ensuite, le Nickel est déposé par électroplaquage. Nous avons noté que le Nickel déposé par la électroplaquage en utilisant la solution de sulphamate de nickel est sujet à moins de stress que le Nickel déposé par évaporation. Ce qui est un facteur favorable à la résistance du Nickel par voie électrochimique lors de l'étape de gravure plasma. La figure 9 montre une image du masque de Ni déposé sur le W.

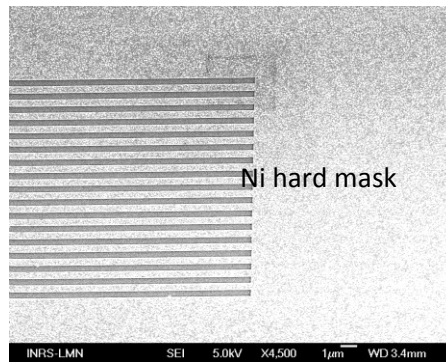


Figure 9: Image MEB du masque de Ni déposé par électroplaquage.

Après le dépôt du masque de Nickel, la résine est enlevée dans un bain (i.e remover), ce qui permet au W de réapparaître en surface, là où le Nickel n'a pas été déposé. Un bâti de gravure RIE-ICP (Oxford PlasmaLab System100) a été utilisé pour les étapes de gravure plasma. Après gravure par plasma du W, la couche de CBN apparaît en surface. Le système de détection optique de fin de gravure (end-point) permet d'arrêter la gravure dès que la couche de W est complètement gravée. Ensuite, lors de la gravure plasma du CBN, le même système permet d'arrêter la gravure dès que la totalité de la couche est gravée. La profondeur de gravure approximative pour les motifs est de 250 nm, avec une vitesse de gravure de 30 nm/min. Enfin l'échantillon est immergé, dans une solution  $\text{NH}_4\text{OH} + \text{H}_2\text{O}_2$  diluée avec de l'eau, pendant quelques heures afin d'enlever le W au-dessus de la couche de CBN non gravée. En utilisant le procédé décrit ci-dessus, nous avons réalisé les motifs pour le réseau et les marques

d'alignement sur les quatre coins de l'échantillon en même temps. Par la suite, les mêmes étapes sont répétées pour la réalisation des guides d'ondes; la résine électronique utilisée dans ce cas est la ZEP520A. Les marques d'alignement sur les coins sont utilisées pour aligner les guides d'ondes avec le réseau.

## **6. Caractérisations du coupleur de réseau**

Un coupleur de réseau avec une période de 400 nm et une profondeur de gravure de 250 nm a été fabriqué. La période et chaque valeur de profondeur ont été calculées sur la base de la technique de simulation reportée en référence [7]. Pour les caractérisations, les coupleurs de réseau sont couplés à la structure des guides d'ondes en CBN, tel que le montre la figure 10.

Sur une table ajustable en XYZ, nous plaçons une puce contenant plusieurs ensembles de coupleur de réseau optique associés à différents guides d'onde en CBN ayant différentes longueurs de guide d'onde. D'abord la lumière est couplée au coupleur de réseau optique à partir d'une source laser 1550 nm. Cette lumière couplée se propage à travers chaque guide d'onde et est découplée à l'autre extrémité par les autres coupleurs de réseau et mesurée par un analyseur.

Une caméra de vue de dessus et une caméra de vue latérale associées au logiciel ViewSonic sont utilisées pour l'alignement de la puce de coupleurs de réseau, l'entrée et la sortie de la fibre.

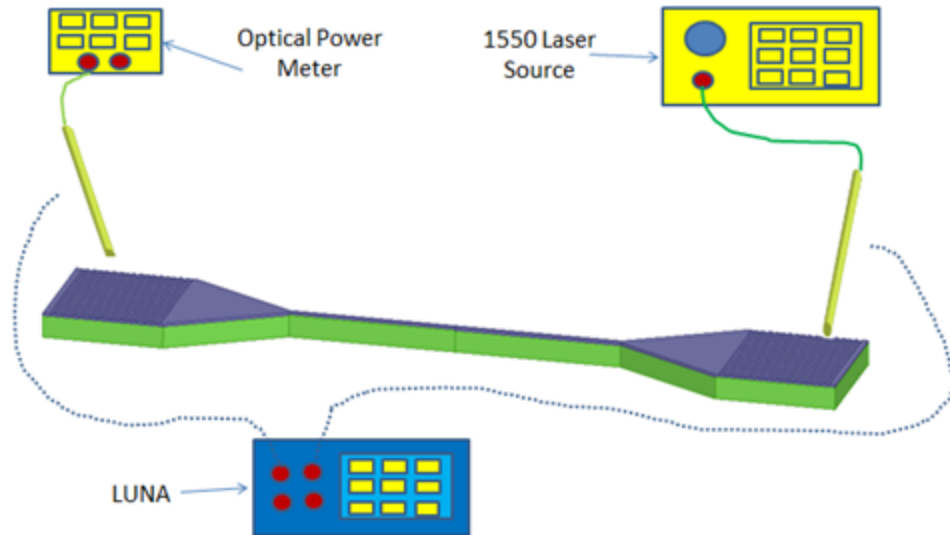


Figure 10: Diagramme bloc du système de caractérisation du coupleur de réseau optique.

L'angle de couplage a été varié de  $7^\circ$  à  $15^\circ$  et la puissance de sortie de la lumière a été mesurée à partir du point où nous avons déterminé un optimum de l'angle de couplage (autour de  $10^\circ$ ). A l'angle optimal de couplage, la lumière pénétrant le coupleur est maximale. Elle se propage par la suite à travers la structure guide d'ondes. Pour chaque composant, la hauteur de l'entrée et la sortie de la fibre est également ajustée pour réduire le bruit.

Une fois que la position du composant, la hauteur entrée/sortie de la fibre et l'angle de couplage sont optimisés, l'entrée et la sortie sont connectées à l'analyseur vectoriel Luna pour mesurer la puissance totale perdue en fonction de la longueur d'onde, tel que montré sur la figure 11 (a). La figure 11(a) montre la mesure de la puissance totale perdue (pertes d'insertion du coupleur + pertes de propagation du guide d'onde) en fonction de la longueur d'onde pour les longueurs de guide d'onde de 2, 4 et 8 mm. Des pertes de puissance de 3 dB sont systématiquement soustraites des mesures.

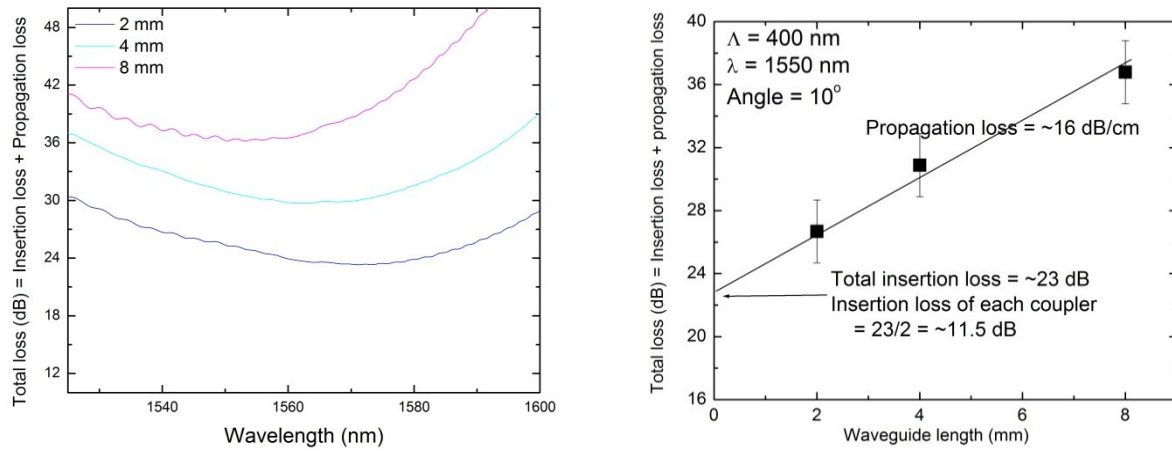


Figure 11: (a) Perte totale en fonction de la longueur d'onde pour différentes longueurs de guide d'onde mesurée par l'analyseur vectoriel LUNA. (b) Perte totale en fonction de la longueur du guide d'onde.

La figure 11 (b) montre les pertes totales en fonction de la longueur du guide d'ondes. Une extrapolation des pertes totales lorsque la longueur du guide d'onde est supposée être zéro donne les pertes totales d'insertion à savoir  $\sim 11.5$  dB par coupleur. Cette valeur est nettement plus élevée que celle des coupleurs à base de SOI conventionnels [7]. Cependant, la possibilité de coupler la lumière dans les guides d'ondes via un coupleur optique intégré au CBN, est prometteur pour l'intégration de ce nouveau matériau pour les applications EO haute performance. A partir de la pente des pertes totales en fonction de la longueur des guides d'onde, des pertes de propagation de 16 dB/cm, qui sont plus élevées que celles obtenues pour les structure guide d'ondes réalisés sur des substrats de MgO ou de Si [7]. Cela pourrait être dû aux fortes rugosités engendrées sur les flancs durant l'étape de gravure.

## 7. Conclusion

A travers ce travail, nous avons optimisé la filière CBN sur substrat GGG. Nous avons démontré expérimentalement la possibilité de réaliser un tel matériau sur ce substrat en optimisant sa cristallinité et sa rugosité. Des couches de qualité épitaxiale et de faible rugosité ont été ainsi obtenues. De plus, nous avons fabriqué avec succès des coupleurs optiques capables de coupler la lumière dans des guides d'onde de ce matériau. . Nous avons mesuré les pertes d'insertion et les pertes de propagation de la structure guide d'onde en CBN comme étant respectivement de  $\sim 11.5$  dB par coupleur et de  $\sim 16$  dB/cm. La possibilité de coupler la lumière dans les guides d'ondes via un coupleur optique intégré au CBN, est prometteur pour l'intégration de ce nouveau matériau pour les applications EO haute performance.

## 8. References

1. R. Helsten, et al., "Pockels response in calcium barium niobate thin films", *Applied Physics Letters*, 91, 261101, (2007).
2. C.L. Jia et al., "Tailoring the orientations of complex niobate films on perovskite substrates", *Acta Materialia*, 54, 9, (2006).
3. S.B. Mi et al., "Growth of  $\text{Ca}_x\text{Ba}_{1-x}\text{Nb}_2\text{O}_6$  thin films on MgO (100) by pulsed laser deposition", *Journal of Crystal Growth*, 291, 243–248, (2006).
4. J.-II Hong, "Room-temperature, texture-controlled growth of ZnO thin films and their application for growing aligned ZnO nanowire arrays", *Nanotechnology*, 20, 085609, (2009).
5. Paul F. Ndione, et al., "Structural and optical properties of epitaxial  $\text{Ca}_x\text{Ba}_{1-x}\text{Nb}_2\text{O}_6$  thin films grown on MgO by pulsed laser deposition", *J. Appl. Phys.* 103, 033510 (2008).
6. S. Vigne, et al., "Structural and optical properties of  $\text{Ca}_x\text{Ba}_{1-x}\text{Nb}_2\text{O}_6$  thin films deposited by radio frequency magnetron sputtering", *Optical Materials Express*, 5, 11, (2015).
7. Faezeh Fesharaki, et al., "Accurate theoretical and experimental characterization of optical grating coupler", *Optics Express*, 24, 18, (2016).